REPORT DOCUMENTATION PAGE

Form Approved OMB NO. 0704-0188

1. REPORT DATE (DD-MM-YYYY)	2. REPORT TYPE	3. DATES COVERED (From - To)
30-08-2022	Final Report	1-Mar-2019 - 31-May-2022

4. TITLE AND SUBTITLE

Final Report: Carrier dynamics and modulation properties of selective area epitaxial quantum structures in dielectric nanophotonic cavities for high speed and energy efficient lasers

5a. CONTRACT NUMBER
W911NF-19-1-0108

5b. GRANT NUMBER

5c. PROGRAM ELEMENT NUMBER
611102
611104

6. AUTHORS

5d. PROJECT NUMBER

5e. TASK NUMBER

5f. WORK UNIT NUMBER

7. PERFORMING ORGANIZATION NAMES AND ADDRESSES

University of Texas at Arlington
701 South Nedderman Drive
Box 19145
Arlington, TX 76019 -0145

8. PERFORMING ORGANIZATION REPORT NUMBER

9. SPONSORING/MONITORING AGENCY NAME(S) AND ADDRESS (ES)

U.S. Army Research Office
P.O. Box 12211
Research Triangle Park, NC 27709-2211

10. SPONSOR/MONITOR'S ACRONYM(S)
ARO

11. SPONSOR/MONITOR'S REPORT NUMBER(S)
74644-EL-H.8

12. DISTRIBUTION AVAILIBILITY STATEMENT

Approved for public release; distribution is unlimited.

13. SUPPLEMENTARY NOTES

The views, opinions and/or findings contained in this report are those of the author(s) and should not contrued as an official Department of the Army position, policy or decision, unless so designated by other documentation.

14. ABSTRACT

15. SUBJECT TERMS

16. SECURITY CLASSIFICATION OF:			17. LIMITATION OF ABSTRACT	15. NUMBER OF PAGES	19a. NAME OF RESPONSIBLE PERSON
a. REPORT	b. ABSTRACT	c. THIS PAGE			Weidong Zhou
UU	UU	UU	UU		19b. TELEPHONE NUMBER 817-272-1227

RPPR Final Report
as of 30-Aug-2022

Agency Code: 21XD

Proposal Number: 74644ELH **Agreement Number: W911NF-19-1-0108**
INVESTIGATOR(S):

Name: Weidong Zhou
Email: wzhou@uta.edu
Phone Number: 8172721227
Principal: Y

Organization: **University of Texas at Arlington**
Address: 701 South Nedderman Drive, Arlington, TX 760190145
Country: USA
DUNS Number: 064234610 EIN: 756000121
Report Date: 31-Aug-2022 Date Received: 30-Aug-2022
Final Report for Period Beginning 01-Mar-2019 and Ending 31-May-2022
Title: Carrier dynamics and modulation properties of selective area epitaxial quantum structures in dielectric nanophotonic cavities for high speed and energy efficient lasers
Begin Performance Period: 01-Mar-2019 **End Performance Period:** 31-May-2022
Report Term: 0-Other
Submitted By: Weidong Zhou Email: wzhou@uta.edu
Phone: (817) 272-1227
Distribution Statement: 1-Approved for public release; distribution is unlimited.

STEM Degrees: 2 **STEM Participants:** 5

Major Goals: The overall project goal is to investigate theoretically and experimentally carrier dynamics and modulation properties of low dimensional quantum structures in heterostructure photonic crystal cavities for high modulation bandwidth and high energy efficient emitters. Selective area epitaxial Quantum dots (SAE-QDs) with high density and high homogeneity will be investigated to potentially unlock the full potentials of these artificial atoms with high quantum efficiency, high differential gain, and temperature insensitive physical properties. The coupling of these SAE-QDs with both traditional and nanoscale dielectric optical cavities will also be investigated with modified spontaneous emission and controlled light-matter interactions for lasers with low lasing threshold, high modulation bandwidth and low damping, high operation temperatures. The ultimate scaling towards attojoule (aJ) energy efficiency and athermal operation will also be analyzed, with strategies in active material volume scaling, strain engineering and optical cavity scaling.

Accomplishments: Over the three year project period, we have carried out the proposed research tasks as listed in the proposal. Specifically, we have made the following acheivements:
(1). Development of programs for rate equation analysis and establishment of the theoretical foundations for the high performance laser cavity design. Our design will have superior cavity performance in terms of low energy cost, high quality factor, and small cavity volume, compared to the current state-of-the-art LEAP laser reported from NTT group.
(2). Design, fabrication and characterization of photinic crystal nanobeam (PCNB) cavities on Si3N4 platform. we proposed a nanobeam cavity with fin structure (US provisional patent filed). We carried out both electrical and optical investigations and achieved cavity designs with improved electrical performance while maintaining excellent optical properties.
(3). Fabrication process development: in order to achieve the proposed nanobeam cavity with fin scheme, the first investigation is SiN based nanobeam cavities with and without fins. We demonstrated the effect of fins on the optical cavity performance. The results have been published.
(4). Characterization of high speed laser: multiple 1.3 um QD edge emitting lasers were fabricated and tested their small signal modulation properties. These demonstration is investating wafer active lawer for future nanobeam laser with fin.
(5). Additionally, phase tuning capabilities is investigated theoretically in photonic crystal cavities. Full 2pi phase shift is feasible based on our study. These results can be incorporated in our laser cavity designs for potential phase based modulations as well. Another patent application is being filed on high speed phase modulations.
(6). We also established new collaborations with researchers in Sandia National Labs, through their CINT user programs, where both cavity scaling and energy efficiency will be investigated through collaborations with Sandia

Researchers.

Training Opportunities: One MS student was supported and graduated.
One PhD student is being supported.
One postdoc is partially supported.
A high school student was also involved in this project.

RPPR Final Report
as of 30-Aug-2022

Results Dissemination: Related publications (Total 22)

Journals (2)
1. M. Pan, Z. Liu, A. Kalapala, Y. Chen, Y. Sun, and W. Zhou, "Complete 2?? phase control by photonic crystal slabs," Opt. Express 29, 40795-40804 (2021)
2. Z. Liu, Y. Chen, X. Ge, and W. Zhou, “Photonic Crystal Nanobeam Cavities with Lateral Fins ", Nanophotonics, 2021 https://doi.org/10.1515/nanoph-2021-0361.

Patent Disclosures (2)
1. W. Zhou and X. Ge, Nanobeam Cavities Having Carrier-Injection Beams, US Patent App. 17/369,789.
2. W. D. Zhou, “High speed spatial light modulators” US provisional patent application (July 2021).

Invited Conference Talks (13)
1. W. Zhou, “Photonic Crystal Silicon Membrane Optoelectronics”, 29th International Conference on Amorphous & Nanocrystalline Semiconductors, Nanjing, China, Aug. 23-26, 2022.
2. W. Zhou, “Scaling of photonic crystal surface emitting lasers”, IEEE Summer Topicals Meeting Series, Cabo San Lucas, Mexico, July 11-13, 2022.
3. W. Zhou, and X. Li, “MacEtch for photonic crystals and optoelectronics”, 22nd IEEE International Conference on Nanotechnology, Palma de Mallorca, Spain, July 4-8, 2022.
4. W. D. Zhou, “Photonic crystal cavity integrated CVD WS2 for attojoule optoelectronics”, Photonics West, 2022.
5. W. D. Zhou, “Photonic crystal lasers and phase modulators for 3D integrated photonics”, Photonics West, 2022.
6. W. D. Zhou, S. Liu, C. Reuterskiöld Hedlund, and M. Hammar, “Scaling of photonic crystal lasers for energy-efficient 3D integrated photonics on silicon (Invited)”, Compound Semiconductor Week (CSW) conference, Stockholm, Sweden, May 17-21, 2021.
7. W.D. Zhou, “Scaling of photonic crystal surface emitting lasers for 3D integrated Membrane photonics (Invited)”, Integrated Optics: Design, Devices, Systems and Applications VI, in the Optics + Optoelectronics Digital Forum 2021, April 19-23, 2021.
8. W. D. Zhou, “Photonic crystal lasers (Invited)”, Frontiers of Optoelectronics New Year Online Workshop, Jan. 23, 2021.
9. W. D. Zhou, “Transfer printing automation for heterogeneous 3D photonic integration (Invited)”, Photonics West, San Francisco, CA, Feb. 4-7, 2020.
10. W. D. Zhou, “Transfer printing automation for heterogeneous 3D photonic integration (Invited)”, MRS Fall Meeting, Boston, MA, Dec. 1-5, 2019.
11. W.D. Zhou, “Hybrid integrated semiconductor photonic crystal lasers”, 12th International Photonics and OptoElectronics Meetings (POEM 2019), November 11-14, 2019, Wuhan, China
12. W. D. Zhou, “Scaling of photonic crystal surface-emitting lasers for 3D photonic integration”, International Conference on Optoelectronic and Microelectronic Technology and Application 2019 (OMTA 2019), Nov. 7-9, 2019, Nanjing, China.
13. W. D. Zhou, “Hybrid integrated semiconductor photonic crystal lasers”, Asia Communications and Photonics Conference 2019 (ACP 2019), Nov. 2-5, 2019, Chengdu, China.

Contributed Conference Talks (5)
1. Z. Liu, M. Pan, A. Liu, G. Kelly, M. Sampsell, J. Liu, and W. Zhou, “Photonic Crystal Slab Metalens”, IEEE Photonics Conference, Vancouver, Canada, Nov. 13-17, 2022. (submitted).
2. A. Liu, M. Pan, Z. Liu, and W. Zhou, “A Reconfigurable Sensing Structure for Fast Optical Modulation by Graphene in Critically Coupled Photonic Crystal Cavities”, IEEE Sensors Conference, Dallas, TX, Oct. 30-Nov. 2, 2022. (submitted).
3. Z. Liu, M. Pan, C. Guo, M. Vasilyev, Y. Sun, and W. Zhou, “Full 2? phase shift from single and double layer photonic crystal slabs”, IEEE Photonics Conference, Oct. 18-021, 2021 (Virtual).
4. Z. Liu, Y. Chen, X. Ge, and W. Zhou, “Photonic crystal nanobeam cavities with lateral fins”, IEEE Photonics Conference, Oct. 18-021, 2021 (Virtual).
5. N. K. Gadiyaram, J. Coleman, and W. Zhou, “Towards Attojoule operation of semiconductor Quantum well Lasers”, IEEE Photonics Conference, Sept. 28-Oct. 1, 2020 (Virtual).

Honors and Awards: Weidong Zhou, OSA Fellow, 2020
Zhonghe Liu, Outstand Student Employee, UTA, 2020.

RPPR Final Report
as of 30-Aug-2022

Protocol Activity Status:

Technology Transfer: Patent Disclosures (2)
1. W. Zhou and X. Ge, Nanobeam Cavities Having Carrier-Injection Beams, US Patent App. 17/369,789.
2. W. D. Zhou, “High speed spatial light modulators” US provisional patent application (July 2021).

PARTICIPANTS:

Participant Type: PD/PI
Participant: Weidong Zhou
Person Months Worked: 2.00 **Funding Support:**
Project Contribution:
National Academy Member: N

Participant Type: Postdoctoral (scholar, fellow or other postdoctoral position)
Participant: Mingsen Pan
Person Months Worked: 10.00 **Funding Support:**
Project Contribution:
National Academy Member: N

Participant Type: Graduate Student (research assistant)
Participant: Zhonghe Liu
Person Months Worked: 6.00 **Funding Support:**
Project Contribution:
National Academy Member: N

Participant Type: Graduate Student (research assistant)
Participant: Nithish Gadiyaram
Person Months Worked: 6.00 **Funding Support:**
Project Contribution:
National Academy Member: N

Participant Type: Graduate Student (research assistant)
Participant: Yudong Chen
Person Months Worked: 12.00 **Funding Support:**
Project Contribution:
National Academy Member: N

Participant Type: High School Student
Participant: Chelsea Takam
Person Months Worked: 2.00 **Funding Support:**
Project Contribution:
National Academy Member: N

Participant Type: High School Student
Participant: Aaron Liu

RPPR Final Report
as of 30-Aug-2022

Person Months Worked: 2.00 **Funding Support:**
Project Contribution:
National Academy Member: N

ARTICLES:

Publication Type: Journal Article Peer Reviewed: Y **Publication Status:** 1-Published
Journal: Optics Express
Publication Identifier Type: DOI Publication Identifier: 10.1364/OE.440687
Volume: 29 Issue: 25 First Page #: 40795
Date Submitted: 6/29/22 12:00AM Date Published: 11/1/21 5:00AM
Publication Location:
Article Title: Complete 2pi phase control by photonic crystal slabs
Authors: Mingsen Pan, Zhonghe Liu, Akhil Raj Kumar Kalapala, Yudong Chen, Yuze Sun, Weidong Zhou
Keywords: Photonic crystal, phase modulation, SOI
Abstract: Photonic crystal slabs are the state of the art in the studies of the light confinement, optical wave modulating and guiding, as well as nonlinear optical response. Previous studies have shown abundant real-world implementations of photonic crystals in planar optics, metamaterials, sensors, and lasers. Here, we report a novel full 2? phase control method in the reflected light beam over the interaction with a photonic crystal resonant mode, verified by the temporal coupled-mode analysis and S-parameter simulations. Enhanced by the asymmetric coupling with the output ports, the 2? phase shift can be achieved with the silicon photonics platforms such as Silicon-on-Silica and Silicon-on-Insulator heterostructures. Such photonic crystal phase control method provides a general guide in the design of phase-shift metamaterials, suggesting a wide range of applications in the field of sensing, spatial light modulation, and beam steering.
Distribution Statement: 1-Approved for public release; distribution is unlimited.
Acknowledged Federal Support: **Y**

Publication Type: Journal Article Peer Reviewed: Y **Publication Status:** 1-Published
Journal: Nanophotonics
Publication Identifier Type: DOI Publication Identifier: 10.1515/nanoph-2021-0361
Volume: 10 Issue: 15 First Page #: 3889
Date Submitted: 6/29/22 12:00AM Date Published: 11/1/21 5:00AM
Publication Location:
Article Title: Photonic crystal nanobeam cavities with lateral fins
Authors: Zhonghe Liu, Yudong Chen, Xiaochen Ge, Weidong Zhou
Keywords: Photonic crystal, nanobeam; nanocavity
Abstract: We present the design, fabrication, and characterization of suspended arrays of small volume, high quality factor (Q) silicon nitride photonic crystal nanobeam (PCNB) cavities with lateral nanorod fin structures. By controlling the alignment position of the fins with respect to the air holes, the resonance wavelength and Q-factor of the PCNB cavities can be tuned to realize the desired performance. Measured tunable range of 2 × 104 and 10 nm is achieved for Q-factor and resonance wavelength, respectively, with the highest Q-factor measured at 2.5 × 104. Incorporating such nanorod fins into the nanobeam cavity is demonstrated to provide improved mechanical support, thermal transport, and channels of lateral carrier injection for the suspended PCNB. The proposed PCNB cavities with lateral fins are advantageous for energy efficient, ultra-compact lasers, modulators, filters, and sensors.
Distribution Statement: 1-Approved for public release; distribution is unlimited.
Acknowledged Federal Support: **Y**

CONFERENCE PAPERS:

RPPR Final Report
as of 30-Aug-2022

Publication Type: Conference Paper or Presentation **Publication Status:** 1-Published
Conference Name: IEEE Photonics Conference
Date Received: 29-Jun-2022 Conference Date: 28-Sep-2020 Date Published:
Conference Location: Virtual
Paper Title: Towards Attojoule operation of semiconductor Quantum well Lasers
Authors: N. Gadiyaram, J. Coleman, and W. Zhou
Acknowledged Federal Support: **Y**

Publication Type: Conference Paper or Presentation **Publication Status:** 1-Published
Conference Name: 2021 IEEE Photonics Conference (IPC)
Date Received: 29-Jun-2022 Conference Date: 18-Oct-2021 Date Published:
Conference Location: Virtual
Paper Title: Photonic Crystal Nanobeam Cavities with Lateral Fins
Authors: Z. Liu, X. Ge, Y. Chen, and W. Zhou
Acknowledged Federal Support: **Y**

Publication Type: Conference Paper or Presentation **Publication Status:** 1-Published
Conference Name: 2021 IEEE Photonics Conference (IPC)
Date Received: 29-Jun-2022 Conference Date: 18-Oct-2021 Date Published:
Conference Location: Virtual
Paper Title: Full 2pi phase shift from single and double layer photonic crystal slabs
Authors: Z. Liu, M. Pan, C. Guo, M. Vasilyev, Y. Sun, and W. Zhou
Acknowledged Federal Support: **Y**

Publication Type: Conference Paper or Presentation **Publication Status:** 5-Submitted
Conference Name: IEEE Sensors Conference
Date Received: Conference Date: 30-Oct-2022 Date Published:
Conference Location: Dallas, TX
Paper Title: A Reconfigurable Sensing Structure for Fast Optical Modulation by Graphene in Critically Coupled Photonic Crystal Cavities
Authors: A. Liu, M. Pan, Z. Liu, and W. Zhou
Acknowledged Federal Support: **Y**

Partners

,

RPPR Final Report

as of 30-Aug-2022

I certify that the information in the report is complete and accurate:
Signature: Weidong Zhou
Signature Date: 8/30/22 5:25PM

ARO Project Final Report

Report Date: August 30, 2022

Title: Carrier dynamics and modulation properties of selective area epitaxial quantum structures in dielectric heterostruture nanophotonic cavities for high speed and energy efficient lasers

PI: Prof. Weidong Zhou, Univ. of Texas at Arlington

Contract: W911NF1910108 (03/2019-05/2022)

PM: Dr. Michael Gerhold

Status of Effort and Summary:

Over the three year project period, we have carried out the proposed research tasks as listed in the proposal. Specifically, we have made the following acheivements:

(1). Development of programs for rate equation analysis and establishment of the theoretical foundations for the high performance laser cavity design. Our design will have superior cavity performance in terms of low energy cost, high quality factor, and small cavity volume, compared to the current state-of-the-art LEAP (λ-Scale Embedded Active Region Photonic Crystal) laser reported from NTT group.

(2). Based on the cavity analysis, we proposed an attojoule laser structures based on photonic crystal nanobeam (PCNB) cavities with lateral fins (US provisional patent filed). We carried out both electrical and optical investigations and achieved cavity designs with improved electrical performance while maintaining excellent optical properties.

(3). Fabrication process development: in order to achieve the proposed nanobeam cavity with fin scheme, the first investigation is SiN based nanobeam cavities with and without fins. We demonstrated the effect of fins on the optical cavity performance. The results have been published.

(4). Characterization of high speed laser: multiple 1.3 μm QD edge emitting lasers were fabricated and tested their small signal modulation properties. These demonstration is investating wafer active lawer for future nanobeam laser with fin.

(5). Additionally, phase tuning capabilities is investigated theoretically in photonic crystal cavities. Full 2π phase shift is feasible based on our study. These results can be incorporated in our laser cavity designs for potential phase based modulations as well. Another patent application is being filed on high speed phase modulations.

(6). We also established new collaborations with researchers in Sandia National Labs, through their CINT user programs, where both cavity scaling and energy efficiency will be investigated through collaborations with Sandia Researchers.

Related publications (Total 22)

Journals (2 published, 2 in preparation)

1. Y. Chen, C. Gautam, N. K. Gadiyaram, J. Kwoean, Y. Arakawa, and W. Zhou, “Scaling of photonic crystal cavities towards attojoule lasers”, (in preparation)

2. Z. Liu, M. Pan, and W. Zhou, “Transmissive photonic crystal slab metalens” (in preparation)
3. M. Pan, Z. Liu, A. Kalapala, Y. Chen, Y. Sun, and W. Zhou, "Complete 2π phase control by photonic crystal slabs," Opt. Express 29, 40795-40804 (2021)
4. Z. Liu, Y. Chen, X. Ge, and W. Zhou, “Photonic Crystal Nanobeam Cavities with Lateral Fins ", Nanophotonics, 2021 https://doi.org/10.1515/nanoph-2021-0361.

Patent Disclosures (2)

1. W. Zhou and X. Ge, Nanobeam Cavities Having Carrier-Injection Beams, US Patent App. 17/369,789.
2. W. D. Zhou and M. Pan, “High speed spatial light modulators” US patent application (July 2022).

Invited Conference Talks (13)

1. W. Zhou, “Photonic Crystal Silicon Membrane Optoelectronics”, 29th International Conference on Amorphous & Nanocrystalline Semiconductors, Nanjing, China, Aug. 23-26, 2022.
2. W. Zhou, “Scaling of photonic crystal surface emitting lasers”, IEEE Summer Topicals Meeting Series, Cabo San Lucas, Mexico, July 11-13, 2022.
3. W. Zhou, and X. Li, “MacEtch for photonic crystals and optoelectronics”, 22nd IEEE International Conference on Nanotechnology, Palma de Mallorca, Spain, July 4-8, 2022.
4. W. D. Zhou, “Photonic crystal cavity integrated CVD WS2 for attojoule optoelectronics”, Photonics West, 2022.
5. W. D. Zhou, “Photonic crystal lasers and phase modulators for 3D integrated photonics”, Photonics West, 2022.
6. W. D. Zhou, S. Liu, C. Reuterskiöld Hedlund, and M. Hammar, “Scaling of photonic crystal lasers for energy-efficient 3D integrated photonics on silicon (Invited)”, Compound Semiconductor Week (CSW) conference, Stockholm, Sweden, May 17-21, 2021.
7. W.D. Zhou, “Scaling of photonic crystal surface emitting lasers for 3D integrated Membrane photonics (Invited)”, Integrated Optics: Design, Devices, Systems and Applications VI, in the Optics + Optoelectronics Digital Forum 2021, April 19-23, 2021.
8. W. D. Zhou, “Photonic crystal lasers (Invited)”, Frontiers of Optoelectronics New Year Online Workshop, Jan. 23, 2021.
9. W. D. Zhou, “Transfer printing automation for heterogeneous 3D photonic integration (Invited)”, Photonics West, San Francisco, CA, Feb. 4-7, 2020.
10. W. D. Zhou, “Transfer printing automation for heterogeneous 3D photonic integration (Invited)”, MRS Fall Meeting, Boston, MA, Dec. 1-5, 2019.
11. W.D. Zhou, “Hybrid integrated semiconductor photonic crystal lasers”, 12th International Photonics and OptoElectronics Meetings (POEM 2019), November 11-14, 2019, Wuhan, China
12. W. D. Zhou, “Scaling of photonic crystal surface-emitting lasers for 3D photonic integration”, International Conference on Optoelectronic and Microelectronic Technology and Application 2019 (OMTA 2019), Nov. 7-9, 2019, Nanjing, China.
13. W. D. Zhou, “Hybrid integrated semiconductor photonic crystal lasers”, Asia Communications and Photonics Conference 2019 (ACP 2019), Nov. 2-5, 2019, Chengdu, China.

Contributed Conference Talks (5)

1. Z. Liu, M. Pan, A. Liu, G. Kelly, M. Sampsell, J. Liu, and W. Zhou, “Photonic Crystal Slab Metalens”, IEEE Photonics Conference, Vancouver, Canada, Nov. 13-17, 2022. (submitted).
2. A. Liu, M. Pan, Z. Liu, and W. Zhou, “A Reconfigurable Sensing Structure for Fast Optical Modulation by Graphene in Critically Coupled Photonic Crystal Cavities”, IEEE Sensors Conference, Dallas, TX, Oct. 30-Nov. 2, 2022. (submitted).
3. Z. Liu, M. Pan, C. Guo, M. Vasilyev, Y. Sun, and W. Zhou, “Full 2π phase shift from single and double layer photonic crystal slabs”, IEEE Photonics Conference, Oct. 18-021, 2021 (Virtual).
4. Z. Liu, Y. Chen, X. Ge, and W. Zhou, “Photonic crystal nanobeam cavities with lateral fins”, IEEE Photonics Conference, Oct. 18-021, 2021 (Virtual).
5. N. K. Gadiyaram, J. Coleman, and W. Zhou, “Towards Attojoule operation of semiconductor Quantum well Lasers”, IEEE Photonics Conference, Sept. 28-Oct. 1, 2020 (Virtual).

Table of contents

1 The State of the Art: LEAP Lasers

In order to achieve energy efficient lasers, scaling in laser cavity is critical. While nanolasers based on metallic cavities have been pursued as the ultimate limit in nanolasers, the efficiency of these lasers are extremely low due to the loss associated with the metallic cavities. On the other hand, dielectric photonic crystal cavities have shown to be a powerful platform in scaling towards the desired volume for attojoule lasers while maintaining high quality factors. Shown in **Fig. 1** is the state of the art summary for different laser cavities. Note that the best laser so far is the photonic crystal LEAP (λ-Scale Embedded Active Region Photonic Crystal) laser reported by NTT group in Japan. They reported different LEAP laser designs to achieve high speed lasers with low energy cost.

On one design with volume of 0.11 μm^3, they achieved energy cost of 10 fJ/bit at 25 Gbps, with WPE of 7.35%. On another design with volume of 0.04725 μm^3, they achieved energy cost of 1 fJ/bit at 10 Gbps, with WPE of 0.19%.

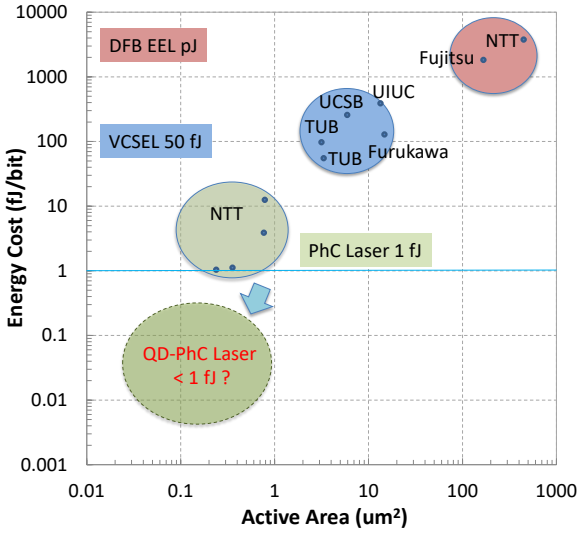

Fig. 1 Laser energy cost state of the art.

Based on these results, we carried out detailed rate equation analysis to figure out the desired laser cavity parameters. Based on the findings, a novel nanobeam cavity with fin structure was also proposed and investigated, for further cavity scaling for sub-fJ/bit operations.

2 Rate Equation Model Analysis

2.1 Rate Equation Basics

The characteristics of semiconductor lasers are governed by the well-known rate equations which describe the coupling, or interaction, of carrier density and photon density [1]. As shown in Fig. 2, it desicribes how to the whole process from injected carriers to emitted photons.

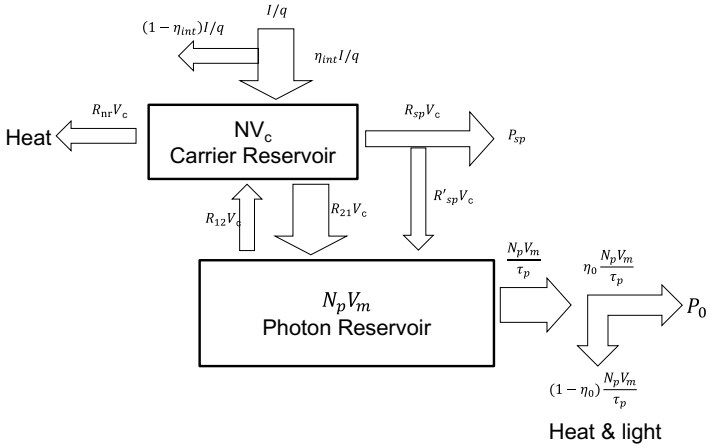

Fig. 2 Rate Equation Process Flow [1]

The rate equations for the carrier density and the photon density in the active region are:

$$V_c\frac{dN}{dt}=\frac{\eta_{inj}I}{q}-\left(R_{sp}+R_{nr}\right)V_c-(R_{21}-R_{12})V_c \quad (1)$$

$$V_m\frac{dN_p}{dt}=(R_{21}-R_{12})V_c+R'_{sp}V_c-\frac{N_pV_m}{\tau_p} \quad (2)$$

where N is the carrier density, N_p is the photon density, V_c is the volume of active region, V_m is the mode volume, I is the injection current, τ_p is the photon lifetime, R_{sp} is the spontaneous recombination rate, R'_{sp} is the spontaneous emission to lasing mode, R_{nr} is the nonradiative recombination rate, R_{21} is the stimulated recombination rate, R_{12} is the absorption recombination rate, η_{inj} is the injection efficiency, I is the injection current, q is elementray charge.

For the carrier density part, the first part ($\frac{\eta_{inj}I}{q}$) means how many carriers inject into the laser system. The next term ($(R_{sp}+R_{nr})Vc$) means how much carriers are lost to nonradiative and spontaneous recombinations. Conisder the Einstein coefficient, the nonradiative and spontaneous part could be coverted to:

$$(R_{sp}+R_{nr})Vc = (AN+BN^2+CN^3)Vc \tag{3}$$

The final term ($(R_{21}-R_{12})Vc$) describes the carriers associated with the absorption (R_{12}) and sitmulated emission processes (R_{21}), which could be disctibed by the laser gain mode ($g(N)$) in terms of net stimulated emission:

$$R_{21}-R_{12} = v_g g(N) N_p \tag{4}$$

Where,

$$g(N) = \frac{g_0}{1+\varepsilon N_p} \ln\left(\frac{N+N_s}{N_{tr}+N_s}\right) \tag{5}$$

g_0 is empirical gain coefficient, N_s is gain coefficient fitting parameters, N_{tr} is transparent carrier density, v_g is group velocity in the active region and ε is Gain compression factor.

For the rate equation of photon density, the first term is the photons generated associated with the net stimulated emission $(R_{21}-R_{12})Vc$. The second term is related to the photons generated from spontaneous emission process which contributes to lasing photons in the cavity:

$$R'_{sp}Vc = \beta R_{sp} = \beta BN^2 \tag{6}$$

The final term ($\frac{N_p V_p}{\tau_p}$) shows the photons lost as the emitted laser power.

Based on the above analysis, we can rewrite the rate equations:

$$\frac{dN}{dt} = \frac{\eta_{inj}I(N)}{qVc} - (AN+BN^2+CN^3) - v_g g(N) N_p(N) \tag{7}$$

and

$$\frac{dN_p}{dt} = \Gamma v_g g(N) N_p + \beta BN^2 \Gamma - \frac{1}{\tau_p} N_p \tag{8}$$

where τ_p is the photon lifetime and $\frac{1}{\tau_p} = \frac{\omega}{Q}$, Γ is the optical confinement factor, β is the spontaneous emission factor.

2.2 Steady-State Performance on Power and Threshold

From equations (7) and (8), we can model and calculate the laser emission response under dynmic and steady-state condition. When we cndier steady-state condition, the carrier and photon densities will be a constant. So, $\frac{dN}{dt} = 0$ and $\frac{dN_p}{dt} = 0$. We can obtain steady-state functions for both

I and P:

$$I(N) = \frac{qVc}{\eta_{inj}}\left(AN + BN^2 + CN^3 + v_g g(N) N_p(N)\right) \tag{9}$$

and

$$P_{out} = \eta_{out}\frac{1}{\tau_p}V_m N_p = \eta_{out}(\eta_i \Gamma v_g g(N) N_p V_m + \beta B N^2 \Gamma V_m) \tag{10}$$

Where $\eta_{out} = Q/Q_c$ is optical output efficiency of the laser. Q is total quality factor of device and Q_c is quality factor contributing to the laser output.

Threshold current is another very important parameter need to be studied. On threshold condition,if we assume that only a small fraction of the spontaneous emsission is coupled into the mode (i.e., β is quite small), then the second term of equation (8) can be neglected:

$$g_{th} = (\frac{1}{v_g \tau_p \Gamma}) \tag{11}$$

Thus, the carrier density on threshold condition is:

$$N_{th} = (N_{tr} + N_s) \cdot exp\left(\frac{g_{th}}{g_0}\right) - N_s \tag{12}$$

Combining euqaitons (9) and (12), threshold current could be consider as:

$$I(N_{th}, N_p) = \frac{qVc}{\eta_i}\left(AN_{th} + B{N_{th}}^2 + C{N_{th}}^3 + v_g g(N_{th}) N_p(N_{th})\right) \tag{13}$$

To validate our model, we first consider the LEAP laser structure [1](cavity length=2.5μm, wdth=0.3μm), and try to compare the simulation results obtained from our model with the results reported. In the simulation, Q_c is fixed at 6,000 and Q factor vary from 100 to 6000. For the output power simulation, the input current is set to be at 0.1 mA. The complete definition of parameters is shown in Table 1 for 1300 nm InGaAs QD material system on GaAs (for nanobeam laser) and 1550 nm InGaAs QW material system on InP (for LEAP laser).

The simulated results based on our model are shown in Fig. 3(b) and Fig. 3(d) for the threshold current and output power, respectively. Shown in Fig. 3(a) and Fig. 3(d) are the simulations results reported in [1] . The results agree very well the publicated ones.

Table 1 Parameters for rate equation analysis.

Symbol	Parameter	Value(InGaAs/GaAs)	Values (LEAP)	Units
A	Non radiative recombination coefficient	Negligible [1]	5.0×10^{8}	s^{-1}
B	Radiative recombination coefficient	0.8×10^{-10} [1]	1.7×10^{-10}	cm^3s^{-1}
C	Auger recombination coefficient	3.5×10^{-30} [1]	1.0×10^{-28}	cm^6s^{-1}
λ	Operating Wavelength	1300	1550	*nm*
T	Temperature	300	300	*Kelvin*
g_o	Empirical gain coefficient	1800 [1]	1742	cm^{-1}

N_s	Gain coefficient fitting parameters	-0.4×10[18] [1]	-1.05 ×10[18]	cm^{-3}
N_{tr}	Transparent carrier density	1.8×10[18] [1]	1.405 ×10[18]	cm^{-3}
c	Speed of light	3.0×10[10]	3.0 ×10[18]	*cm/s*
ε	Gain compression factor	1.5×10[-17] [1]	3.0 ×10[17]	cm^3
V_{bi}	Built in potential	0.7 [2]	0.6	*Volt*
v_g	Group velocity in the active region	0.7143×10[10] [1]	0.78 ×10[10]	*cm/s*
q	Electron charge	1.602×10[-19]	1.602×10[-19]	*Coulo*
R_s	Series resistance of the laser	5191	29×10[3]	*Ohm*
Γ	Optical confinement factor	~0.195	0.03	---
η_{inj}	Carrier injection efficiency	0.8 [1]	0.4	---
η_{out}	Optical output efficiency of the laser	Q/Qc	Q/Qc	---

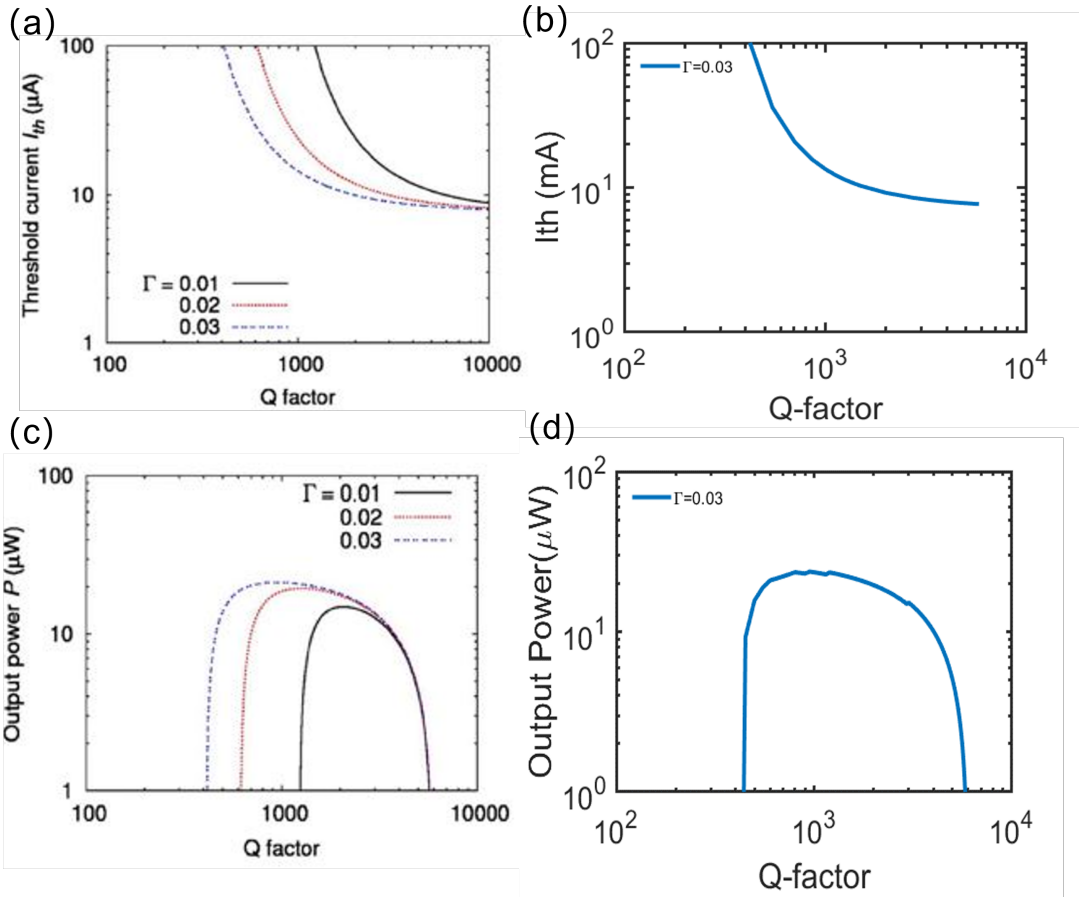

Fig. 3 Threshold Current and Output Power Simulation Comparisons. (a) Threshold current simulation of the LEAP laser. (b) Threshold current simulation based on our model under $\Gamma = 0.03$. (c) Output power simulation of the LEAP laser under input current I_{in}=0,1mA. (d) Output power simulation of our model under $\Gamma = 0.03$ and I_{in}=0.1mA.

2.3 Dynamic Performance and Efficiency Estimate

To further explore the electrical and optical performance of lasers, the relation between a small-signal modulation of injection current and the laser output power can give us more insights

about the operation properties, such as bandwidth, energy cost, and wall-plug efficiency (WPE). To study the operation speed and energy cost of semiconductor lasers, let us start from the relaxation effect of the photons and carriers. Under a small-signal perturbation, the relaxation resonance frequency (f_r) of a laser can be described as [1]

$$f_r = \frac{1}{2\pi}\sqrt{\gamma_{nn}\gamma_{pp} + \gamma_{np}\gamma_{pn}} \tag{14}$$

Where,

$$\gamma_{nn} = \frac{\partial\left(R_{nr} + R_{sp}\right)}{\partial N} + \frac{\partial G}{\partial N}N_p, \qquad \gamma_{pp} = -\left(\Gamma G + \Gamma\frac{\partial G}{\partial N}N_p - \frac{1}{\tau_p}\right)$$

$$\gamma_{pn} = \Gamma\frac{\partial G}{\partial N}N_p + \Gamma\frac{\partial R_{sp}}{\partial N}, \qquad \gamma_{np} = G + \frac{\partial G}{\partial N}N_p$$

And then, the 3dB resonance frequency is:

$$f_{3dB} = \sqrt{\frac{-\left(\frac{\gamma_{pp}}{2\pi}\right)^2 + 2{f_r}^2 + \sqrt{(\frac{\gamma_{pp}}{2\pi})^4 - 4(\frac{\gamma_{pp}}{2\pi})^2{f_r}^2 + 8{f_r}^4}}{2}} \tag{15}$$

Thus, the 3dB bandwidth is:

$$B = 1.3f_{3dB} \tag{16}$$

As we discussed previously, 3dB bandwidth and ouput power will impact each other. In order to optimize the output power and speed response, A figure of merit (FOM) function was introduced [1]:

$$FOM = B \cdot P_{out} \tag{17}$$

The injection power (P_{in}) for the laser is

$$P_{in} = V_{bi}I + I^2R_s \tag{18}$$

The energy cost (E_c) in this report is defined as the power consumption divided by modulation speed of the laser,

$$E_c = \frac{P_{inp}}{1.3\ f_{3dB}} = \frac{V_{bi}I + I^2R_s}{1.3\ f_{3dB}} \tag{19}$$

where f_{3dB} is the 3-dB bandwidth of the laser, and 1.3 f_{3dB} corresponds to the non-return-to-zero (NRZ) signal modulation bandwidth.

Therefore, the WPE of a laser is defined as

$$WPE = \left(\frac{P_{out}}{P_{inp}}\right) \times\ 100\ \% \tag{20}$$

Similar procedures were taken to simulate the 3dB modulation bandwidth and FOM parameters for different Q factors, as shown in Fig. 3(b) and Fig. 4 (d), respectively. Shown in Fig. 3(a) and Fig. 4(c) are the reported simulation results from LEAP lasers. [1] The results agree very well also.

Efficiencies were also simulated based on our model. The simulation is based on the LEAP laser structure (wdth=0.3μm). Q_c is fixed at 6,000 and Q factor is fixed at 2,000. Cavity size is changed by chaing the device length (L) only. The resistance is related with L as R=ρ/L, where resistivity ρ= $10000\Omega \cdot \mu m$. The results are shown in Fig. 5. For each subplot, the left one is reported results, and the right one is simulation result from our model. Fig. 5 (a), (c), (e) and (g) are simulations with 1mW input electron power. Fig. 5 (b), (d), (f) and (h) are simulations with 10mW input electron power. Obviously, all our simulation results are matched with LEAP laser reported results. So, our simulation mode could work to simulation output power, threshold current, 3dB repsone, FOM and energy cost with differernet Q factors and different structures.

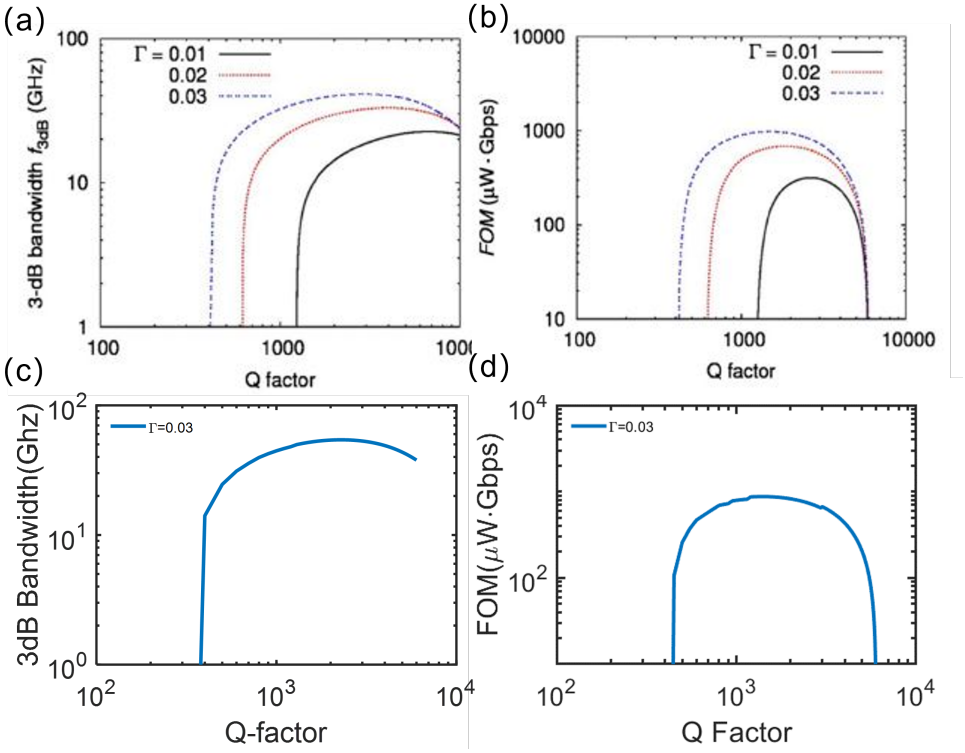

Fig. 4 3dB Bandwidth and FOM Simulation Comparison. (a) 3dB response simulation of LEAP mode under input current Iin=0,1mA. (b) 3dB response simulation of our mode under $\boldsymbol{\Gamma = 0.03}$ and Iin=0.1mA. (c) FOM simulation of LEAP mode under input current Iin=0,1mA. (d) FOM simulation of our mode under $\boldsymbol{\Gamma = 0.03}$ and Iin=0.1mA

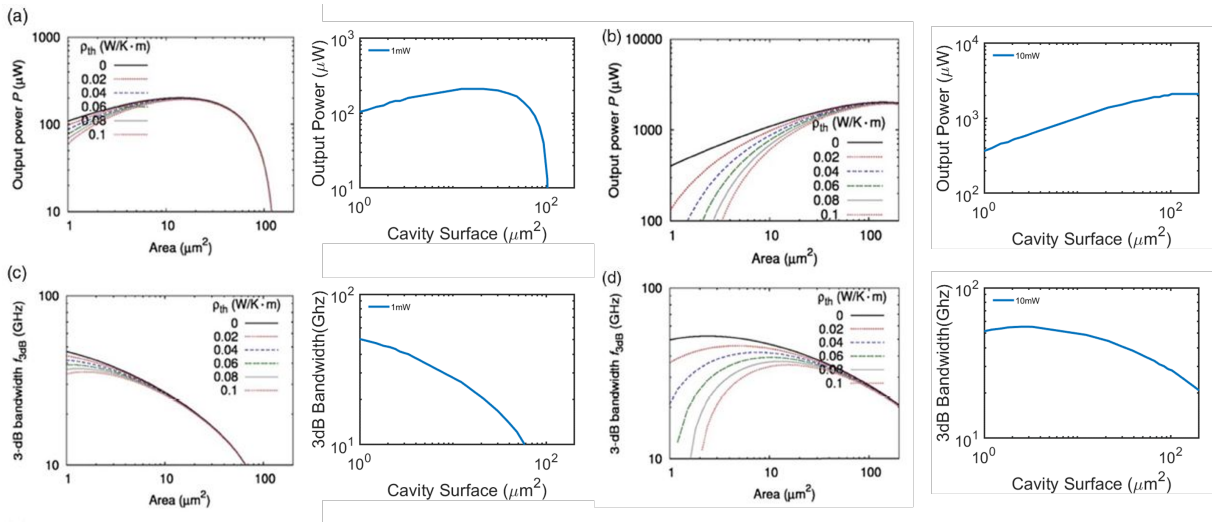

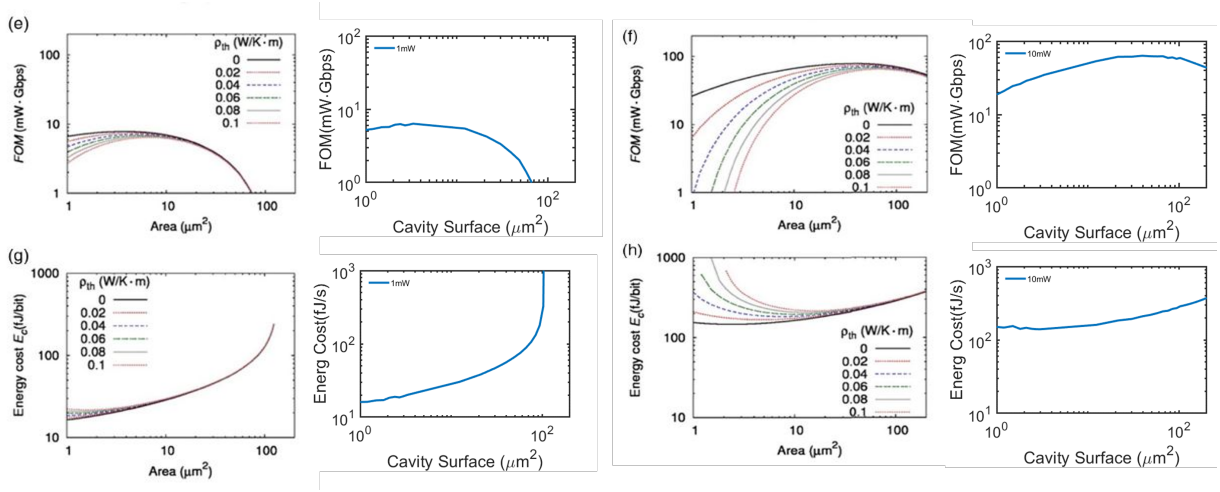

Fig. 5 Laser Specification Variation with Different Device Strcutre size Change.(a) Output power simulation reported by LEAP(left) and our mode (right) with 1mW input electrical power. (b) Ouput power simulation reported by LEAP(left) and our mode (right) with 10mW input electrical power.(c) 3dB response simulation reported by LEAP(left) and our mode (right) with 1mW input electrical power. (d) 3dB response simulation reported by LEAP(left) and our mode (right) with 1mW input electrical power. (e) FOM simulation reported by LEAP(left) and our mode (right) with 1mW input electrical power. (f) FOM simulation reported by LEAP(left) and our mode (right) with 10mW input electrical power. (g) Energy cost simulation reported by LEAP(left) and our mode (right) with 1mW input electrical power.(h) Energy cost simulation reported by LEAP(left) and our mode (right) with 10mW input electrical power.

2.4 Conditions for attojoule lasers

In order to find out the cavity design conditions for attojoule lasers, we investigated both the impact of the cavity volume V_c and cavity confinement factor Q.

2.4.1 Impact of the cavity volume V_c

We first consider the impact of the cavity volume on the laser performance by assuming a fixed cavity Q of 10,000. The results are shown in Fig. 6. We first consider 1,550 nm InP based material system, the threshold current decreases with the reduction in the the cavity volume. However, there is an optimal cavity volume for optimal wall plug efficiency, as shown in the shaded area in Fig. 6(a), at V_c=0.1-0.8 μm^3. At the same volume region, the laser has high 3dB bandwidth and lowest energy cost (1fJ/bit) (Fig. 6(b)).

Similar trends can be found for 1,300 nm GaAs material system (Fig. 6(c,d)), with the optimal cavity volume changed slightly (V_c~0.07-0.7 μm^3). The minimal energy cost achieved here is 0.6 fJ/bit.

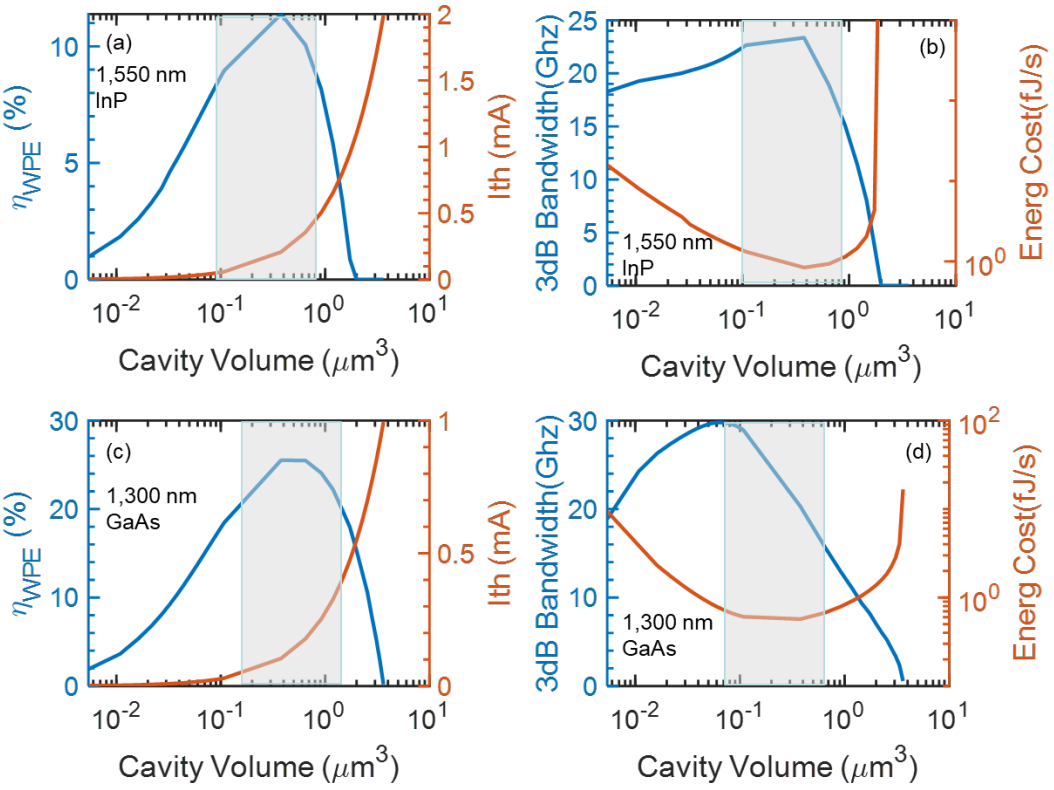

Fig. 6. Impact of cavity volume V_c on: (a, c) wall plug efficiency and threshold, and (c, d)energy cost and 3dB bandwidth. (b, d). The simulation is done underQ=10,000 and 1mA input current conditions. Both InP (a, b) at 1,550 nm and GaAs (c, d) at 1,300 nm) are considered.

2.4.2 Impact of cavity quality factor Q

To achieve low energy cost with moderate operation bandwidth, the cavity Q-factor and confinement factor should be taken into careful consideration. In this section, we consider two material systems with two types of laser cavities.

(i) Reference cavity: 1,550 nm QW based LEAP lasers as reported by NTT group [1];

(ii) Target cavity: 1,310 nm QD based nanobeam lasers proposed here.

Due to the larger overlapping with the active material, a strong optical confinement can reduce the threshold current, and enhance laser output power, and thus improve the modulation speed. On the other hand, high Q-factor can limit the bandwidth due to the strong damping effect. Assume the cavity Q factor fixed at 200,000 to make sure the total Q could sweep from 2,000 to 200,000. We investigate the cavity design requirements with respect to the goal of minimal energy cost. Based on the results shown in Fig. 6, for lowest energy cost, we set the cavity volume Vc=0.0217 μm^3. Shown in **Fig. 7** are the simulated laser performance results for 1,550 nm InP based QW material system (**Fig. 7** (a,b) and 1,310 nm InGaAs GaAs based QD material system (**Fig. 7** (c,d)). For both material systems, the lasing threshold reduces with the increase of the cavity Q factors. Accordingly the wall-plug efficiency (WPE) increases with the increase of the Q factors. Both wall plug efficiency and threshold reach saturation beyond Q factor of 40,000. This suggest that lasing cavity Q factor should be designed to be in the range of 10,000's.

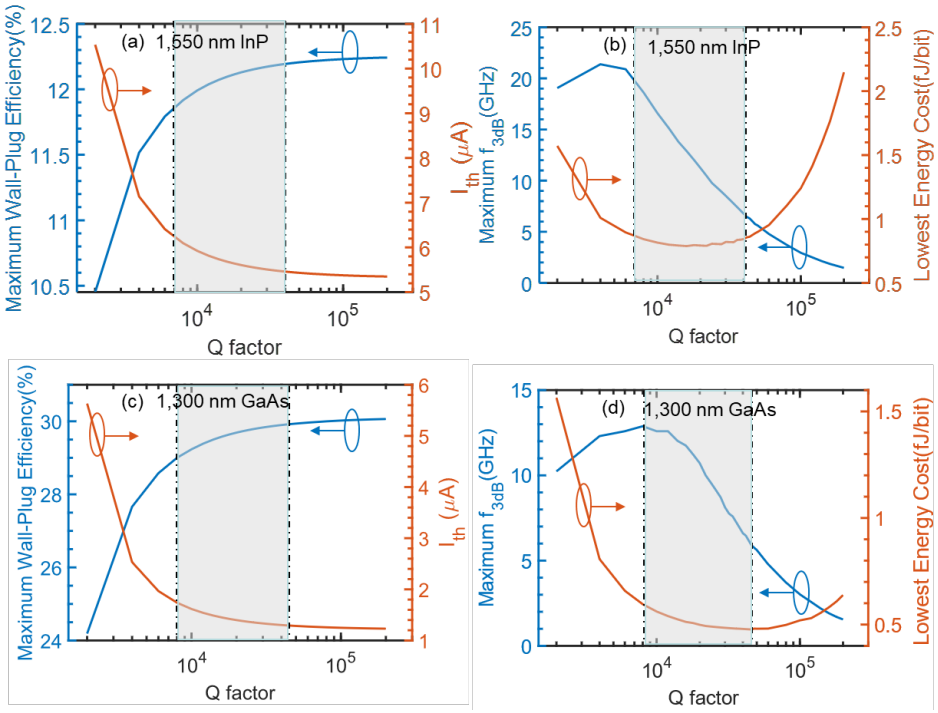

Fig. 7 Impact of cavity Q factors on: (a, c) wall plug efficiency and threshold, and (c, d) energy cost and 3dB bandwidth. The simulation is done under Vc= 0.0217μm^3,V_m= 0.1113 μm^3.(The shaded regions correspond to a laser device that has lower energy cost .

On the other hand, there exists optimimal Q factor ranges for both 3dB bandwidth and energy cost, as shown in **Fig. 7** (b,d). At first, increasing Q factors up to 7-8,000, 3dB bandwidth increases and energy cost reduces. However, further increase in Q factor results in reduction in 3dB bandwidth. Energy cost remains low until Q factors increased to 40-50,000. To achieve low energy cost while maintaining larger bandwidth, we can obtain a range of the Q-factor by trading off between the two parameters. The Q-factor regions between these critical points (shaded areas) indicate that the cavity can have a lower energy cost and higher bandwidth, which is our criterion for the cavity design (show in the shaded region in Fig. 7). The minimum energy cost and maximum bandwidth of our cavity are shown in Table 2**.** Compared with LEAP laser (by NTT group, shown in the last column of report (Table 2), the threshold current with the nanobeam design in this report is 2.8μA (or 68.5% lower) and energy cost is 0.48 fJ/bit (or 50.3% lower). Therefore, our design strategy can achieve better electrical performances in terms of the energy cost and threshold current.

In summary, we investigated the cavity design conditions for sub-fJ/bit (attojoule) lasers. It is possible to achieve 0.5-0.6 fJ/bit operation from a 1,300 nm QD material system with wall plug efficiency of 30% and threshold current of 1.29 μA. However the 3dB bandwidth is limited to only 6-13 GHz. On the other hand, higher speed lasers (13-21 GHz) can be achieved from an 1550 nm InP material based lasers, though the energy cost is higher (0.8-1 fJ/bit) and the wall plug efficiency is also lower (12%). The threshold is also higher (5.68 -7 μA).

Table 2 Electrical Performance of the Nanobeam Laser.

	1,300 nm InGaAs QD		1,550 nm InGaAsP QW		1,550 LEAP [3]
Optimization Target	**Energy Cost**	**3dB Bandwidth**	**Energy cost**	**3dB Bandwidth**	**Energy Cost**
Q-factor	4.6×10^4	8,000	1.6×10^4	4,000	2.3×10^4
Cavity Volume V_c (μm^3)	0.0217	0.0217	0.0217	0.0217	0.0038
Mode Volume V_m (μm^3)	0.1113	0.1113	0.1113	0.1113	0.0422
Γ	0.195	0.195	0.195	0.195	0.03
Energy cost (fJ/bit)	0.48	0.6	0.8	1.01	0.96
3dB bandwidth (GHz)	5.9	12.9	12.88	21.38	-
WPE (%)	29.9	29	12.1	11.52	-
Threshold current (μA)	1.29	1.74	5.68	7.14	4.1

3 Proposed Nanobeam Laser Cavities with Fins

3.1 Introduction

During the last several decades, the field of photonic crystal have seen drastic developments in both theory and application [4-8]. Scaling of optical cavities has been of great interests for future high performance, low energy consumption and high-speed optical devices such as semiconductor lasers, light emitting diodes, optical sensors, and modulators. Nanobeam cavity, among other microcavities, has drawn stronger attention for its superior characteristics of ultra-compact size, extreme low mode volume (V), and high quality (Q) factor [9-12]. These characteristics have made nanobeam cavity a competitive candidate for nano lasers, on-chip modulators, optical switches, and filters [13]. In the past decade, nanobeam cavity on III-V platform has achieved lasing threshold of 2.3 μW by optical pumping [14] and 5 μA by electrical pumping [15]; Integrated lasers on silicon nitride nanobeam cavity have also demonstrated to be promising options for lasers on Si [16, 17]. Nanobeam modulators on Si and Si integrated platforms have reached footprint of a few μm^2 [18] in experiment and have potentials to realize high modulation speed larger than 100 GHz at the energy efficiency below fJ/bit theoretically [19, 20]. Nanobeam based optical switches utilize thermo-optic (TO) [21], Electro-optic effect [22], and Kerr nonlinearity [23] have been of growing interests for its simplicity in fabrication. On-chip nanobeam sensors can obtain figure of merit >2, 000 for label free sensing, one order higher compared to other PC sensors [24].

However, the natures of ultra-high performance nanobeam resulted from deep etching [25] and suspending [26] also compromises the implementation of nanobeam structures. Current nanobeam cavities have non-negligible trade-offs in electrical/optical/mechanical/thermal efficiencies due to the required high index contrast cladding and suspended structure. Earlier, non-suspending tunable nanobeam cavities were reported with one-sided nano-tentacles (connecting fins) that improves thermal conductivity and tunability [27]. Other configurations of vertical supporting structure were also proposed that offers electric injection for nanobeam lasers [15].

In this work, we propose and investigate a suspended silicon nitride PCNB cavity with lateral nanorod fin structures on both sides of the nanobeam cavity, where the alignment of the fin position

is tunable to achieve a range of desired Q-factor and resonance wavelength. We also compare the optical performances of the very same PCNB with and without fins. The PCNB structures are shown schematically in Fig. 8(a) and Fig. 8(c), for PCNBs without and with fin structures, respectively. Shown in Fig. 8(b) and Fig. 8(d) are scanning electron micrographs (SEMs) for PCNBs without and win fins, respectively. Compared to the traditional suspended nanobeam cavity, the introduction of the lateral fins improves the mechanical strength, thermal conduction, and electrical carrier injection of the suspended PCNB cavity.

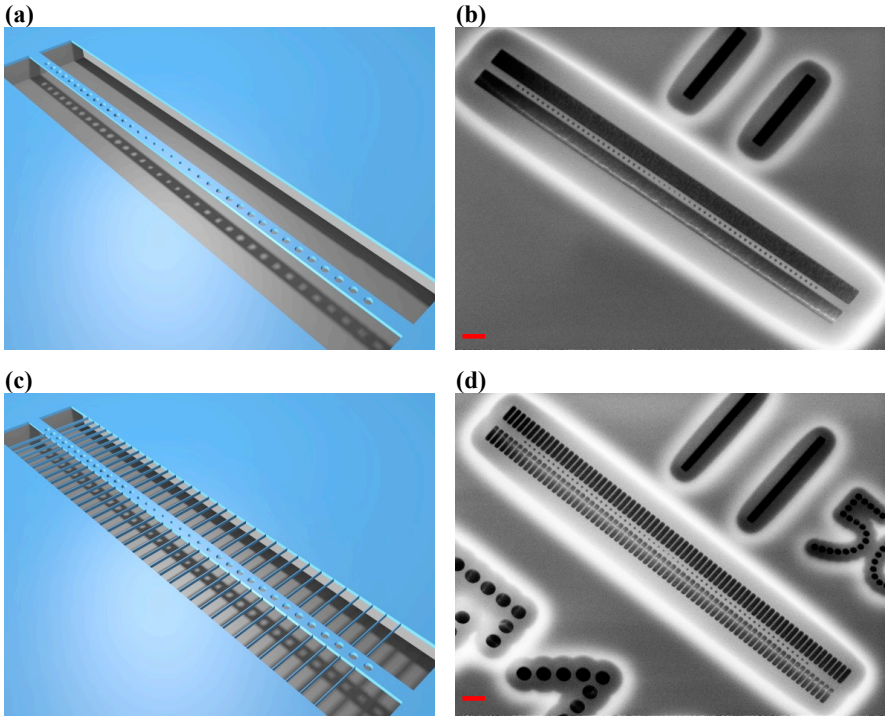

Fig. 8 (a), (c) Schematic illustrations and (b), (d) Scanning electron micrographs of the suspended nanobeam cavity without, and with fin structures, respectively. Scale bars in (b) and (d) are 1 μm.

3.2 Optical Design of Nanobeam Lasers

To implement ultralow energy cost and ultrafast information processing, we have shown earlier that a moderate mode Q-factor (~10^4), modal volume, and higher confinement factor are the key factors. In the current microlaser technology, bandgap defect states in nanobeam structures have higher Q (~10^6) while maintaining a low mode volume (~0.09 μm^3) [28]. Equipped with the lateral current injection scheme, reference [2, 29] demonstrate nanobeam cavities with mode volume of 0.02 μm^3. Starting with the nanobeam design, we simulate the optical performances with MEEP and COMSOL Multiphysics. The schematic of the design is shown in Fig. 9. The initial nanobeam cavity design is a suspended nanobeam cavity. The air holes with uniform spacing are designed outside taper region to serve as Bragg mirrors and provide mode confinement [2, 30], as shown in Fig. 9. A gradually increasing air hole radius in the taper region introduces the adiabatic change of effective refractive index to reduce the mode scattering and enhance mode confinement more effectively.

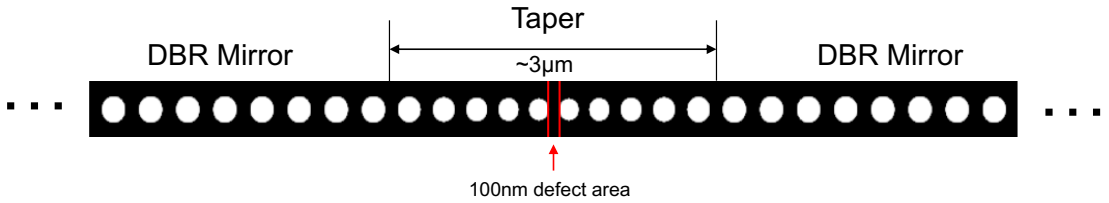

Fig. 9 Schematic of a Nanobeam Cavity Design. The nanobeam cavity is formed by a defect region surrounded by tapered air holes and confined by the DBR mirrors. A 100nm defect area can support a fundamental mode at the wavelength of 1300nm.

The thickness of our GaAs quantum dot (QD) wafer is 230 nm (**Table 3**). The defect resonance mode is designed on the dielectric band and light will be mainly concentrated at the dielectric region (Fig. 10) for better overlapping with the buried MQWs. To design a nanobeam cavity with higher Q at a resonance wavelength around 1300 nm, we optimize its structural parameters such as lattice constant, air hole filling ratio, number of air holes in the taper region, waveguide width, and defect region length. The width of the nanobeam design in Fig. 9 is 450nm, where the fundamental mode is optimized for a near-maximal Q-factor. We focus on the fundamental mode due to its better optical confinement and higher-quality communication. In the taper region, there are 5 air holes with linearly changed periodicity a=263 nm, 275 nm, 287 nm, 298 nm, and 310 nm in each side of the mirror plane (total 10 air holes in the taper region). The lattice constant and air filling ratio of the air hole array for the Bragg mirrors is a=322 nm and r/a=0.305, respectively. The defect region of the nanobeam cavity has a length of 100 nm to support a fundamental mode at λ=1284 nm with a quality factor of $7.8*10^5$, a mode volume in physic region (defined in [28]) of 0.0206 μm^3 and a confinement factor is 0.195.

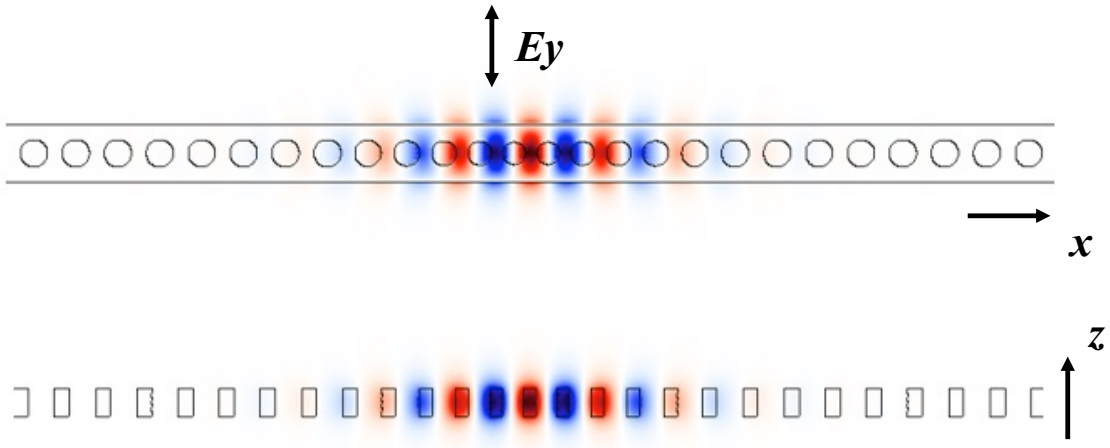

Fig. 10 Ey Filed Distribution of the Fundamental TE Mode in the Nanobeam Cavity.

Table 3 Three-Layer Quantum Dots Heterostructure [29].

Layer	Material	Thickness	QD(InAs) density	Index
spacers	GaAs	56nm	-	3.406
strain-reducing	In(0.15)Ga(0.85)As（InAs dots）	6nm	~300 dots/μm^2	3.4601

spacers	GaAs	50nm	-	3.406
strain-reducing	In(0.15)Ga(0.85)As（InAs dots）	6nm	~300 dots/μm^2	3.4601
spacers	GaAs	50nm	-	3.406
strain-reducing	In(0.15)Ga(0.85)As（InAs dots）	6nm	~300 dots/μm^2	3.4601
spacers	GaAs	56nm	-	3.406
Sacrificial	Al(0.95)Ga(0.05)As	1000nm	-	-
Substrate	GaAs (n)	-	-	3.406

3.3 Photonic crystal nanobeam cavity design

The PCNB cavity is designed to utilize the maximum mirror strength in the 1-D PC, thus it is desirable to have a symmetric radius taper of 6 periods on each side about the center of the cavity according to the deterministic method [31]. As shown in Fig. 11(a), two different parabolic radius tapers are fabricated, one with taper radius changing from 46.9 *nm* to 66.8 *nm* (taper01, red square), and another with taper radius changing from 52.8 *nm* to 69.2 *nm* (taper02, blue circle), to verify the mirror strength theory. Fig. 11(b) shows all the key design parameters for PCNB with fins, including cavity thickness t, PC non-taper regular radius r, PC lattice constant a, fin width w, beam width W_b, and the fin alignment position D. We define D=0 for fins aligned to the center point of 2 airholes, as shown by the solid fins; and D=0.5a for fins aligned to the center of each airhole, as shown by the transparent fin. The optimized values by the deterministic recipe in [31] for these parameters are r =71.8 *nm*, a =272 *nm*, w=30 *nm*, t=150 *nm* and W_b=300 *nm* for the target resonance wavelength at 660 *nm*.

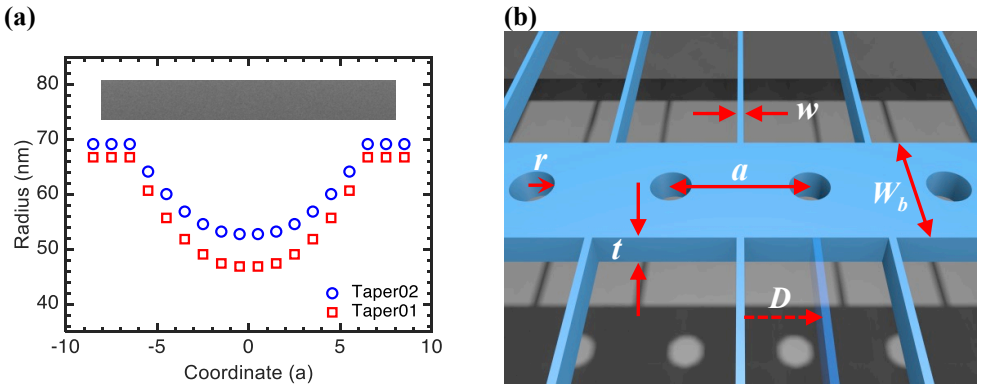

Fig. 11 (a) Fabricated radius taper of the nanobeam cavity (inset is the SEM image of the taper part, and (b) defining parameters of the nanobeam cavity, the dashed arrow and the transparent fin illustrate the fin position shift in the cavity array.

Previous work by J. Zhang [27] has demonstrated that the presence of an optimized lateral tentacle structure on one side of the cavity has minimal effect on the optical performance of the cavity. To investigate impact brought by the presence of fins on both sides of our PCNB cavities, we explored 2 scenarios of nanobeam cavity in numerical simulation as shown in Fig. 12: a suspended nanobeam (a) without and (b) with fins; and a nanobeam cavity on SiO_2 substrate (c) without and (d) with fins. Simulations are performed with the finite-difference time-domain (FDTD) method, using an open-source software package [32]. It shows that the presence of fins

on our PCNBs also has minimal impact to the mode distribution in the cavity and brings less than 2% change in Q-factor when fins are thin (~0.1a) and aligned to the electric field minima. This is verified by the experimental data shown later.

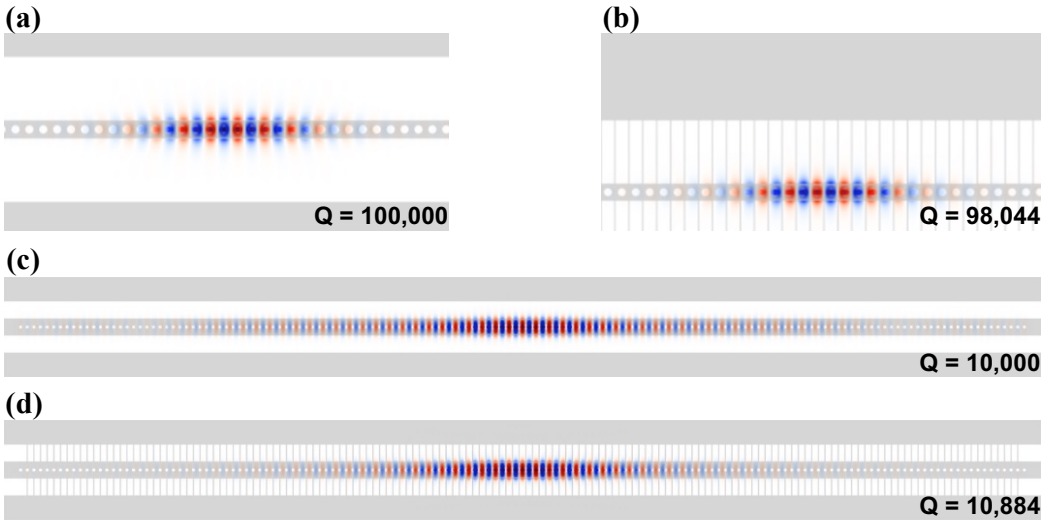

Fig. 12 Comparison of simulated E_y component of the electrical field distribution and quality factor of suspended Si_3N_4 nanobeam cavity (a), without and (b), with lateral fins (fin width 0.1a, 2nd order band edge of air mode)., and of Si_3N_4 nanobeam cavity on SiO_2 substrate (c), without and (d), with lateral fins (fin width 0.2a, 1st order band edge of dielectric mode).

3.4 Fabrication and measurement

3.4.1 Fabrication

The fabrication process of the PCNB cavities includes Si_3N_4 film deposition on Si wafer and PCNB cavity pattern lithography. The 150 nm thick Si_3N_4 film is stoichiometrically grown with low pressure chemical vapor deposition (LPCVD) method at 770°C on p-type silicon wafer in a Tystar Tytan nitridation furnace. The patterning of PCNB cavity consists of standard electron beam (e-beam) lithography (EBL), directional reactive ion etching (RIE) of Si_3N_4 layer, isotropic RIE of Si substrate, stripping and plasma cleaning of the e-beam resist.

The EBL process starts from spin coating (4000 rpm, thickness 371 *nm*) of e-beam resist (ZEP 520A), followed by pre-baking at 180°C for 3 minutes, and afterwards e-beam exposure under accelerating voltage of 20 kV on the Nanometer Pattern Generation System (NPGS, by J. C. Nabity Lithography Systems). The exposed pattern is then developed by Amyl Acetate under refrigeration temperature for 60s followed by a post-baking at temperatures heating up from 60 °C to 100 °C.

The PCNB pattern on the e-beam resist is then etched onto the Si_3N4 layer by inductively coupled reactive ion etching (IPC-RIE) process, at gas flow rate ratio of SF_6: CHF_3: He = (1: 2.5: 2.77), with resulted aspect ratio of 5.3. A following isotropic IPC-RIE process with only SF_6 gas etches the Si substrate to create the suspension of the PCNB on Si_3N_4. The residues of e-beam resist are then dissolved in N-Methyl-2-pyrrolidone (NMP) solution heated up to 75 °C. The suspended thin fins are proved to be intact during this wet process, but the mostly used combination

step of ultrasonication is completely prohibited. Instead, a final process of oxygen plasma ashing for 1 hour completely cleans up all the remains of e-beam resist.

3.4.2 Measurement and analysis

For the nanobeam cavity design without lateral fins, two different tapers are fabricated and compared on the same 1-dimensional (1-D) PC structure, with the taper profiles shown Fig. 11(a). The resonance wavelength of the 1-D PC is determined by the photonic band diagram, as shown in Fig. 13(a) where the air band (solid lines) and dielectric band (dashed lines) are plotted for 1-D PCs with different *r*/*a* ratios. For the target wavelength at 660 *nm*, *r*/*a*=0.27 is picked. The fabricated cavity resonance is then measured by optically pumping the Si_3N_4 cavity with a 450 *nm* laser to activate the defect states in the Si_3N_4. Shown in Fig. 13(b) is the measurement result of cavities where a series of radius offset is scanned to achieve the target device dimension. For both tapers, the resonance wavelength shifts linearly, with Q-factor maximizes near the optimized radius. Taper02 has a closer match of radius profile to the optimized design and the optimized cavity resonance spectrum is shown Fig. 13(c). The highest Q-factor obtained is 2.3×10^4 with full width at half maximum (FWHM) of 28pm. Shown in the inset is the full spectrum measured. Fig. 13(d) shows the SEM image of taper02.

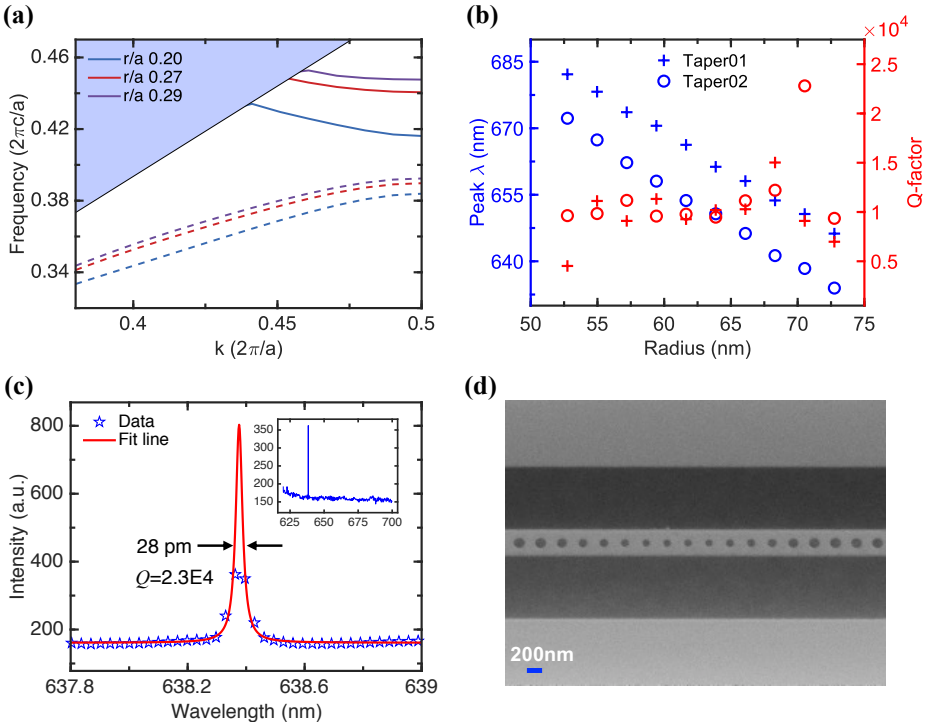

Fig. 13 (a) Photonic band plot of 1-dimentional photonic crystal structure for *r*/*a* ratio of 0.2, 0.27, and 0.29, shaded region is the light cone of Si_3N_4. (b) measured resonance wavelength and quality factor of two different taper structure at different radius offsets. (c) measured optical emission spectrum around the resonance peak and its Lorentzian fitting (inset is the full range spectrum) of one nanobeam cavity without fin that has the same radius as the cavity with fins. (d) top view SEM of the taper region on the suspended nanobeam cavity without fins.

After confirming the cavity radius taper profile, arrays of nanobeam cavities with fins are fabricated with fin alignment varies from the center point of 2 airholes (defined as *D*=0) to the

center of each airhole (defined as D=0.5a). At D=0, the presence of fin rod has minimal influence on the distribution of the electromagnetic (E&M) field distribution compared to non-fin nanobeam cavity, as shown in the measured spectrum in Fig. 14(a), where the measured Q=2.46×10^4 and FWHM=26 *pm*. The true Q-factor can be higher since the resolution on our testing setup is limited to resolve finer peaks. This is close to the result shown in Fig. 13(c) and agrees well with the simulation result described in the previous section. As the fin position shifts to the center of each airhole, the E&M field starts to couple to the lateral rod. As a result, the confinement (Q-factor) in the cavity is reduced and the resonance shifts to lower frequency (higher wavelength). The measured result is shown in Fig. 14(b), where the red (blue) dashed line is the Q-factor (resonance wavelength) of the nanobeam cavity with the same dimension but without fins. It agrees well with the simulation result shown in Fig. 14(c). The lower Q-factor in the measured result is due to both fabrication defects and measurement setup limit.

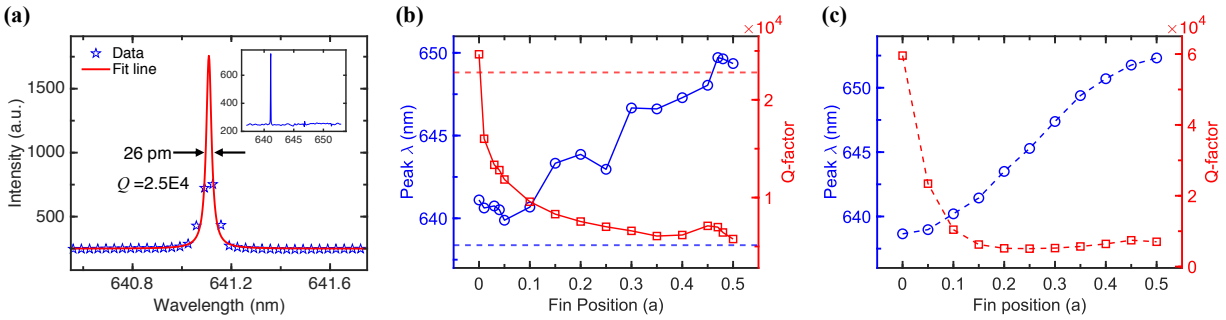

Fig. 14 (a) Measured optical emission spectrum around the resonance peak and its Lorentzian fitting of the nanobeam cavity with fins aligned to the center of 2 airholes, (b) measurement result of tuning of resonance wavelength and Q-factor as fin alignment position changes, where position D=0 is when fins are aligned to center of 2 airholes and position D=0.5 is when fins are aligned to airholes, (c) simulated result of tuning Q-factor and resonance wavelength by changing fin alignment position.

To find out the influence of fabrication offsets in the airhole radius, fin width, and more importantly, the resonance tuning capability of the fin-tuning nanobeam cavity array, another series of PCNBs is fabricated where the radius and fin width offsets are scanned. Shown in Fig. 15(a, b) are the measured resonance wavelength and Q-factor on PCNBs with airhole radius and fin width varies independently. For both D=0 and D=0.5a alignments, there is an optimized airhole radius and an optimized fin width. The variations of radius or fin width around the optimized design (r = 64.5 nm and w = 24.2 nm) cause the Q-factor and resonance wavelength change gradually, which agrees with the numeric simulation results shown in Fig. 15(c, d) in general. The minor discrepancies may be related to the fabrication variations. For both radius and fin width that are 10 nm away from the optimized design value, the Q-factor drops to about half of the optimized Q-factor. It is worth mentioning that the range of wavelength tuning by fin position broadens for larger airhole radiuses and for wider fins. But the broader tuning range comes with a reduced Q-factor in both cases.

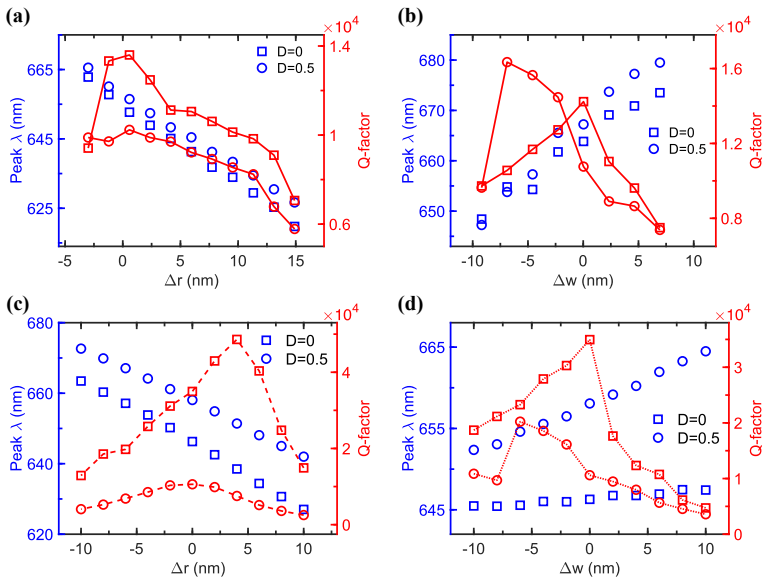

Fig. 15 (a) Measured and (c) Simulated resonance wavelengths and *Q*-factors with different radius offsets; (b) Measured and (d) Simulated resonance wavelengths and *Q*-factors with different fin width offsets.

3.5 Electrical Design of Nanobeam Laser

To consider an efficient current injection scheme for excitation of the defect lasing mode in this cavity [29, 33], we consider the impact of number of fins on the electrical performance.

We first investigate the impact of lateral fins on the series resistance, which will in turn impact the overall energy cost. Different injection fin numbers have different cross section areas and hence different series resistance. 3D full structure simulations of different current injection schemes are carried out with COMSOL semiconductor module. Fig. 16 (a) shows simulated carrier density distributions under 2 current injection schemes: along the nanobeam waveguide (top) and through 4-fin injection (bottom). The n-dopant and p-dopant density are 1.8×10^{18} cm^{-3}, and the red-color region in Fig. 16 (a) is n-dopant region, and blue-color region is p-dopant region. For the side current injection in. the intrinsic region at the cavity center has a 500nm width. For the lateral current injection with fins, the whole beam region is considered as the intrinsic region.

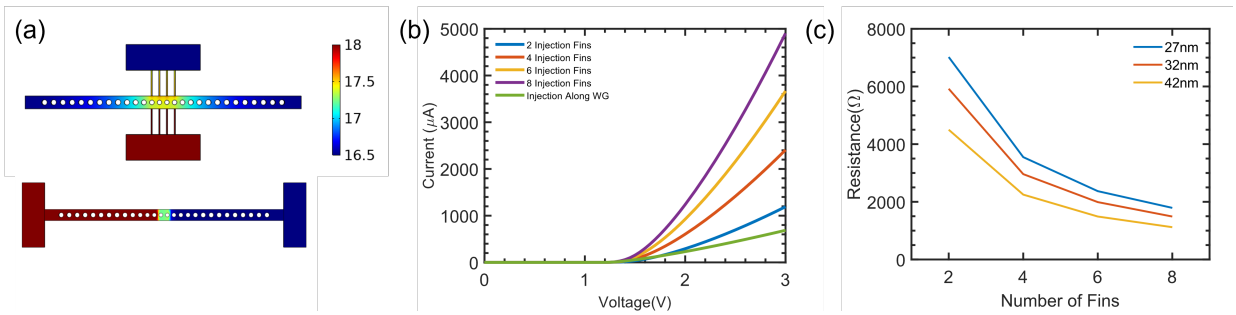

Fig. 16 The simulated impact of lateral fins on the charge injection series resistance: (a) Simulated charge distributions for a 4-fin injection scheme (top) and traditional injection along nanobeam waveguide scheme (bottom); (b) Simulated IV curves with different number of injection fins with fin width of 32 nm. Traditional along waveguide injection IV is also shown for comparison. And (c) Series resistances with different number sand widthes of injection fins.

Fig. 16 (b) shows the IV curves with different current injection schemes with fin width of 32 nm. Based on the simulated IV curves, series resistances are extracted and the results are shown in Fig. 16(c). The series resistance decreases with more injection fins and wider fin widths. However, as shown later, wider fin width will result in the reduction in optical cavity quality factor. Considering the fabrication constraints, we set a fin width of 32 nm.

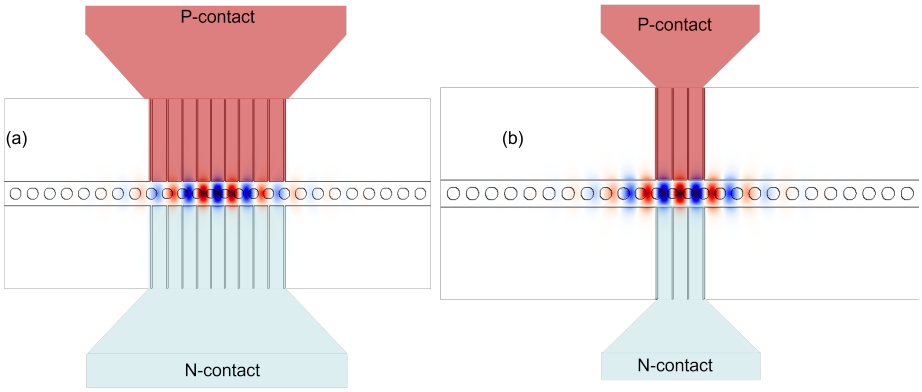

Fig. 17 Schematic of electrical injection through fins structure. The background in the cavity region shows the Ey field distribution (TE mode) of the defect state.(a) The 10-fin injection shecmem. (b) The 4-fin injection scheme.

Then we consider the impact of number of fins on the overall laser performance. As shown in Fig. 17, different number of fins may result in different effective active region (cavity volume) and the overlap with the optical cavity. Here the cavity Q factor is assumed to be 4.6×10^4 (corresponding to the lowest energy cost with 10 injection fins). 10-fin injection scheme is first considered, as shown in Fig. 17 (a), in order to have the injection region cover all the field region. However this design results in relatively large active region, which is not favorable for minimizing energy cost. We then pursued a 4-fin injection scheme as shown in Fig. 17 (b). In this design, we place fins in the center taper region to inject electrons into cavity region.The Q-factor decreases a little due to the light scattering effect by the fins. Considering the Q-factor and the fabrication constraints, the fin width is designed at about 32 nm. With 3D FDTD simulation, a defect resonant mode at λ=1289 nm can be obtained with quality factor of $Q=8.4*10^4$, mode volume of 0.0215 μm^3 and confinement factor of 0.195. However, modes with very high Q will result in reduced 3-dB bandwidth and the output power [34]. Therefore, the optical impacts of the lateral fin structures on the electrical properties are negligible if the cavity design is optimized with these tradeoffs.

The simulated impact of number of fins is shown in Fig. 18. As shown in Fig. 18(a), the active cavity volume Vc scales uniformly with the number of fins. This is related to the uniform increase in the the injection width, as illustrated in the insets of Fig. 18(a). The carrier density distributions (insert plots Fig. 18 (a)) are simulated with COMSOL Multiphysics semiconductor module. The n-dopant (bottom fin region) and p-dopant (top fin region) densities are $1.8*10^{18}$ cm^{-3}. The regions inside the red frame are the active regions defined by such current injection scheme through the fin structure. We assume that the current density mainly concentrates within the red frame, corresponding to the black dash lines in Fig. 18. The optical confinement factor, on the other hand, scales with the number of the fins at gradually reduced steps. This is due to the fact that the optical field distribute is peaked at the center cavity region.

Accordingly, the change of optical mode volume (Vm) and lasing threshold (Ith) also scale with the number of fins, as shown in Fig. 18(b) and Fig. 18(c), respectively. The optical mode volume is calculated based on the confinement factor equation $\Gamma = V_c/V_m$, which is the ratio of

the active region volume and optical volume.

Finally, shown in Fig. 18(d) are the energy cost and WPE, which scale with different number of fins. It is noted that the minimal energy cost (0.1 fJ/bit) and the maximum WPE (34%) occur at 2-fin configuration. The simulation results show that the nanobeam cavities with 2-fin and 4-fin injection regions have the minimal optical volume for low-energy operations. Because a 1-fin structure will reduce the Q factor drastically, we consider the injection fin number is larger than 2.

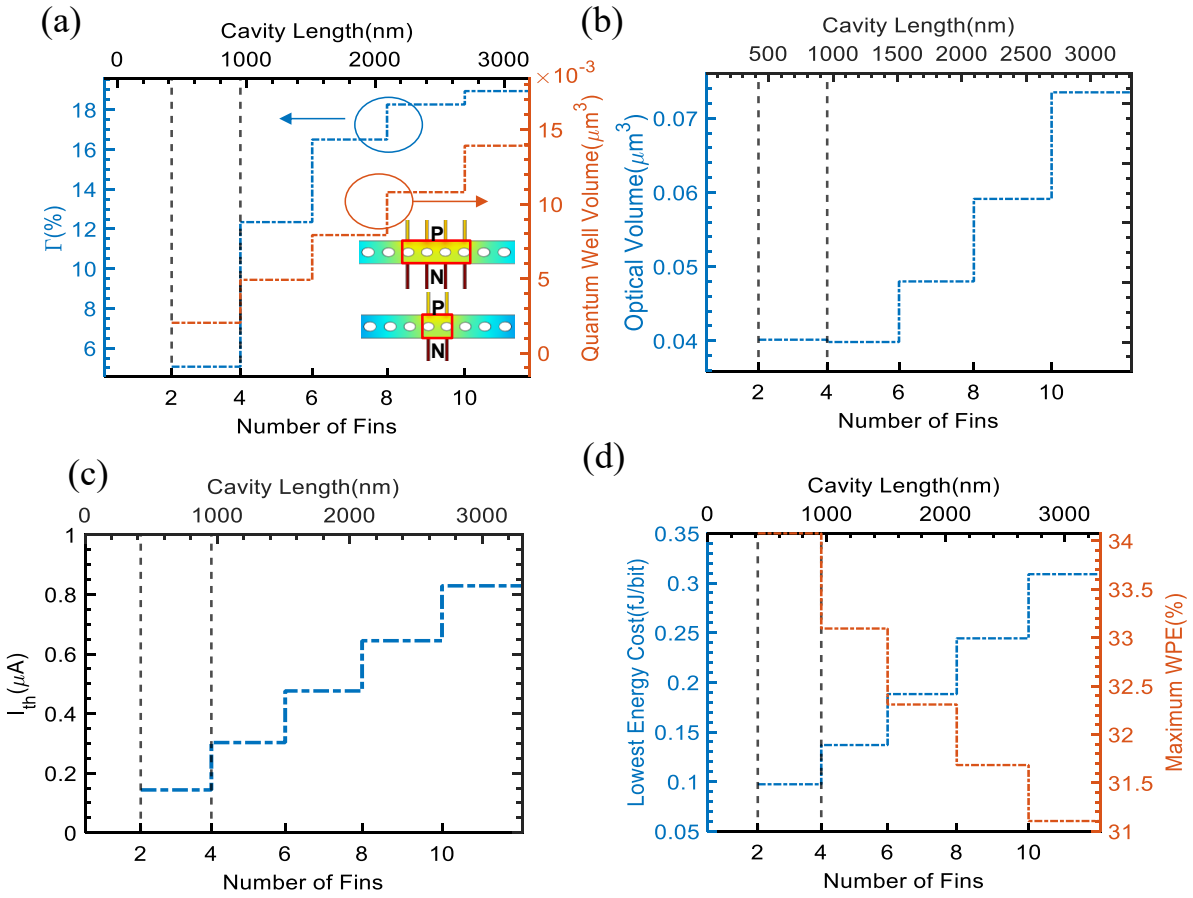

Fig. 18 The impact of number of lateral fins on lasing performance: (a) The change of optical confinement factors and active cavity volumes Vc; (b) The change of optical cavity mode volume Vm; (c) The change of lasing threshold Ith; and (d) The change of energy cost and WPE. Also shown in the insets are the carrier density distributions of 2-fin injection and 4-fin injection schemes.

As listed in **Table 4**, in comparison with the LEAP laser report, the mode volume of our design is 25% smaller, and confinement factor is two times stronger. Therefore, our nanobeam structure are the better candidate for lower energy cost and higher 3dB bandwidth for speed response.

Table 5 shows the electrical performance with 2-fin injection and 4-fin current injection. Traditional nanobeam cavity without fin is also listed as "0-fin (WG)" case for comparison. One of the major impact of the lateral fin design is the drastically reduced active cavity volume by a factor of 10. Also the series resistance also reduced by a factor of 2. This results in ~ five times reduction in energy cost.

Comparing with LEAP laser report (last column in Table 2), the threshold current for the nanobeam design in this report is 3.956μA (or 96.5% lower) with 2-fin injection and 3.797μA (or

92.6% lower) with 4-fin injection, which is also comparable to the previous low-threshold photonic crystal design (287nA [6]); our energy cost is 0.863 fJ/bit (89.9% lower) with 2-fin injection and 0.823fJ/bit (85.7% lower) with 4-fin injection. Therefore, much better electrical performances can be achieved by reducing the injection fin numbers (active region volume).

Table 4 Optical Performance Comparison between LEAP and Nanobeam Design.

	Nanobeam Laser in this Report		**LEAP Photonic Crystal Laser (NTT)**	
Cavity	Without Lateral Fins	With Lateral Fins	Large Region [35]	Reduced Region
Target	1.3μm		1.55μm	
Cavity Volume Vc	0.0217	0.0217	0.0135	0.0038
Mode Volume Vm	0.1113	0.1131	0.15	0.0422
Q	7.8×10^5	8×10^4	2.75×10^5	10^6
Γ	0.195	0.195	0.03	0.03
Wavelength	1284 nm	1289 nm	1558 nm	1534 nm

Table 5 Electrical Performances of the Nanobeam Laser with Different Injection Fins.

Number of fins	0 (WG)	2	4
Q-factor	4.6*10	$4.6*10^4$	$4.6*10^4$
Cavity Volume Vc (μm3)	0.0217	0.0021	0.0049
Mode Volume Vm (μm3)	0.1113	0.04014	0.0398
Confinement Factor (%)	19.5	5.25	12.3
Series Resistance Rs (Ω)	8,000	6,000	3,000
Energy cost (fj/bit)	0.48	0.097	0.137
WPE (%)	29.9	34.1%	33.1%
Threshold current (μA)	1.29	0.144	0.303

3.6 Summary

We designed, fabricated, and measured arrays of nanobeam cavity with lateral fins where the fin alignment position is tuned to control the resonance Q-factor and wavelength. The lateral fins can provide mechanical support, act as thermal conduction channels, and enable carrier injection to the suspended nanobeam cavity. These low mode-volume, high Q-factor nanobeam cavities are ideal candidates for novel lasers, light emitting diodes, optical modulators, filters, and sensors. The nanobeam cavity can also be applied on different materials and can be integrated with new photonic/electronic on-chip platforms for high speed, low power consumption applications.

It is worth mentioning that the proposed structure can be designed to have extremely high Q factors or moderate Q factors depending on the application requirements. The impact of the lateral fins

may be very small (2%) to the nanobeam cavity Q factors. So extremely high Q factors can be achieved. This could be useful for high speed modulators or high sensitivity sensors. On the other hand, moderate Q factors are desirable for nanobeam lasers if we consider trade-offs in modulation speed and energy cost.

Compared with the conventional nanobeam cavity lasers, the proposed nanobeam with fin cavities can result in ~ 5x reduction in energy cost, with minimal value of 0.1 fJ/bit at 2-fin configurations. This offers a promising lasing cavity for attojoule applications.

4 Phase Control Design

Phase control could help us improve the eyes pattern of NRZ signal at high-speed laser modulation for the application in optical communications. Photonic crystal slabs are the state of the art in studies for the light confinement, optical wave modulating and guiding, as well as nonlinear optical response. Previous studies have shown abundant real-world implementations of photonic crystals in planar optics, metamaterials, sensors, and lasers. Here, we report a novel full 2π phase control method in the reflected light beam over the interaction with a photonic crystal resonant mode, verified by the temporal coupled-mode analysis and S-parameter simulations. Enhanced by the asymmetric coupling with the output ports, the 2π phase shift can be achieved with the silicon photonics platforms such as Silicon-on-Silica and Silicon-on-Insulator heterostructures. Such photonic crystal phase control method provides a general guide in the design of phase-shift metamaterials, suggesting a wide range of applications in the field of sensing, spatial light modulation, and beam steering. The full content in this section is available for further review in arXiv.org [36].

In a 2-port system, the dynamic equations for a resonance on a photonic crystal slab (PCS) with an amplitude **a** read,

$$\frac{da}{dt} = \left(j\omega_0 - \frac{1}{\tau}\right)a + \kappa s_+ \tag{19}$$

$$s_- = Cs_+ + ad \tag{20}$$

where $\mathrm{s}_+ = [s_{1+}\ s_{2+}]^{\mathrm{T}}$ and $\mathrm{s}_- = [s_{1-}\ s_{2-}]^{\mathrm{T}}$ are the input and output field amplitudes to the two ports, respectively. The PCS resonant mode couples with incoming waves s_+ with coupling constants $\boldsymbol{\kappa} = [\kappa_1\ \kappa_2]$ and the outgoing waves s_- with coefficients $\mathrm{d} = [d_1\ d_2]^{\mathrm{T}}$. **Eq. (19)** and Eq. **(20)** describe the temporal coupling for mode **a** with resonant frequency ω_0 and life time $1/\tau$ with the background scattering matrix **C**. Determined by the constraints set by the scattering matrix unity and time-reversal symmetry, the total scattering matrix can be derived as

$$S = C + \frac{dd^T}{j(\omega - \omega_0) + \frac{1}{\tau}} \tag{21}$$

The first term in the complex-valued scattering matrix **S** represents the background scattering of light waves, while the second term shows the resonant mode interacting with the background scattering via the coupling term **d**.

The parameters in a symmetric system are $|d_1|^2 = |d_2|^2 = 1/\tau$ and the enhancement factor is $\Gamma = 1$. The scattering matrix of this symmetric structure can be further simplified, considering a special form of background scattering matrix $\mathrm{C} = exp(i\theta)\begin{bmatrix} r & it \\ it & r \end{bmatrix}$,

$$S_{11}(\omega) = exp(i\theta)\left\{r - \frac{1/\tau}{i(\omega-\omega_0)+1/\tau}(r \pm jt)\right\} \quad (22)$$

where the $\pm$ sign denotes the parity of the resonant mode. It can be deduced that $S_{11}(\boldsymbol{\omega})$ evolves with the incoming wave frequency and passes 0 point on its complex plane when $\boldsymbol{\omega = \omega_0 \pm \frac{t}{r}(1/\tau)}$. The phase shift cannot cover the full 2π range in the reflection spectrum because the phase singularity creates a discontinuity or a sudden jump in the reflection phase. At the phase singularity point, the reflectance drops to 0 due to the destructive interference between the resonant mode and the background reflection.

A vertically symmetric structure does not support a 2π phase shift due to the singularities in the reflection or transmission spectra. To pursue a 2π phase shift, it is necessary to remove the phase singularities (i.e., reflection zero or transmission zero). Here, we study the enhanced mode coupling for reflected wave in heterostructures. The reflection phase change can be derived by the S_{11} parameter, and the transmission phase change is governed by the S_{21} parameter.

$$S_{11}(\omega) = C_{11} + h(\omega)|d_1|^2 \quad (23)$$

$$S_{21}(\omega) = C_{21} + h(\omega)d_2^* d_1 \quad (24)$$

where $h(\boldsymbol{\omega}) = \frac{1}{j(\boldsymbol{\omega}-\omega_0)+1/\tau}$ is the lineshape function of the PCS resonant mode. The reflectance and transmittance spectra are in a Fano lineshape. With the complex analysis of the S-parameters, a sufficient condition for 2π phase change in reflected wave can be derived as (also see supplementary section 1),

$$|d_1|^2 > \frac{|r|}{|h(\omega)|} \quad (25)$$

Eq. (25) shows that a 2π phase shift for the reflected wave can be achieved in a structure that has stronger mode coupling amplitude d_1. Another constraint is the energy conservation, $|d_1|^2 + |d_2|^2 = 2/\tau$. In a symmetric 2-port system, the mode profile decays equally to the two ports and the coupling constants are $|d_1|^2 = |d_2|^2 = 1/\tau$. However, for a heterostructure, the mode extends to the two ports asymmetrically. To describe the asymmetric coupling under the energy conservation constraint, we define a reflection coupling enhancement factor as

$$\Gamma = \frac{|d_1|^2}{|d_2|^2} \quad (26)$$

The factor shows the asymmetricity of outgoing energy of the mode to the two ports of the PCS structure. We can further derive a general condition for 2π phase shift in reflection as $\Gamma > 1$ or $|d_1|^2 > 1/\tau$ (see supplementary note 1). To engineer a robust phase shift device, the objective function to optimize the system to achieve a 2π phase shift is to maximize Γ.

In Reference [36], we have shown that, in a symmetric system, we cannot achieve a continuous 2π phase shift due to the existence of the phase singularities. By introducing the asymmetric design, the phase shift by the PCS can be effectively controlled and optimized for different purposes of applications.

5 High speed QD edge emitting Lasers

In this section, we present the fabrication and characterization of an electrically pumped

waveguide edge-emission laser (EEL). We collaborate with Arakawa Group for the quantum dot growth on GaAs wafer. This section presents the fabrication and testing of the benchmark EEL with the quantum dot wafer. The same techniques can be readily applied to our low-cost high-speed laser by the nanobeam cavity designs.

Fig. 19 shows schematic and scanning electron microscope (SEM) pictures from the side view of the EEL and **Table 6** shows layer specification. The EEL is a ridge waveguide on the GaAs substrate with the quantum dot layer lying near the vertical center of the waveguide. The SEM image shows the cleaving results of the wafer at the waveguide facet region.

Table 6 Quantum Dot Wafer Information (Arakawa Group).

Material	Al Content x	Thickness [nm]	Dopant Density [cm^{-3}]	Repeat
p-GaAs	-	100	Be: 2×10^{19}	1
	-	300	Be:1.4×10^{19}	
p-AI(x)Ga(1-x)As	0.2	20	Be:1.4×10^{19}	
	0.4	1000	Be:7×10^{19}	
	0.4	400	Be:4.2×10^{17}	
GaAs	0.2	20	Be:4.2×10^{17}	
	-	20	-	
Quantum dot active layer	-	40		8
GaAs	-	60		1
n-Al(x)Ga(1-x)As	0.2	20	Si:6×10^{17}	
	0.4	1400	Si:6×10^{17}	
	0.2	20	Si:6×10^{17}	
n-GaAs	-	300	Si: 1×10^{18}	
n-GaAs Substrate	-	-	Si: 1-1.5 $\times10^{18}$	

The full fabrication flow for the EELs on the quantum dot wafer from the Arakawa Group is shown in Fig. 20**.** The process starts with p-contact metal deposition for the current injection into the semiconductor laser. We deposit photon resist (NR9-1500PY) on top of the wafer by spin coating followed by UV exposure with photomask to form the p-metal pattern, and then we deposited p-contact metal layer (Pd/Zn/Pd/Au alloy) using e-beam evaporation. The second step is p-mesa etching, including photolithography with photon resist (1813 G2) and p-mesa mask, and reactive ion etching. The third step is n-mesa etching which is the same as p-mesa etching, and we need to etch through active layer. The fourth step is n-contact metal deposition which is the same as p-contact metal deposition. The fifth step is passivation where we deposited oxide layer to insulate the p-metal and n-metal. The final step is the interconnect metal deposition by e-beam evaporator.

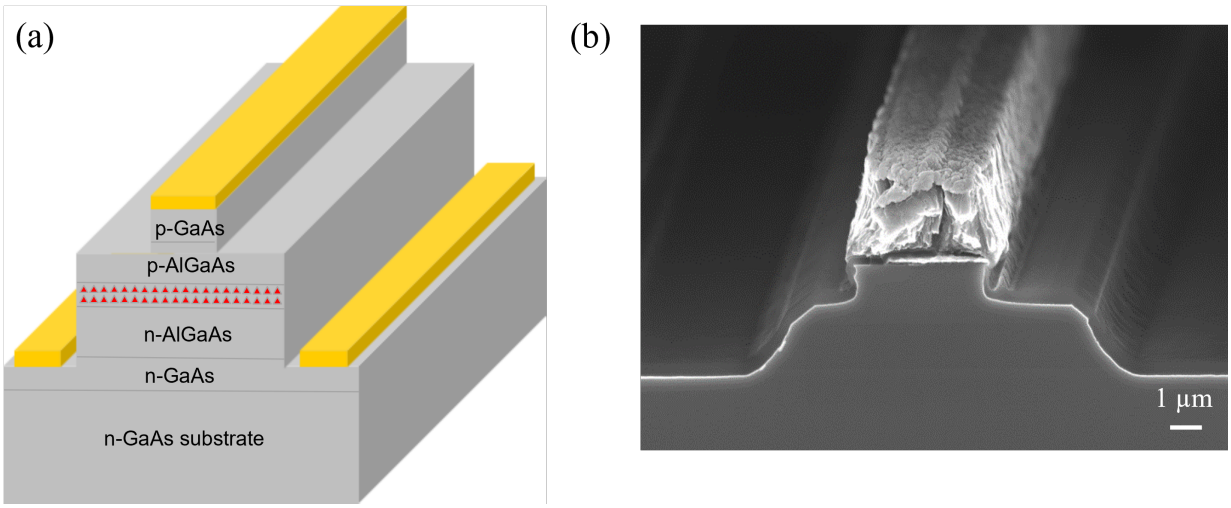

Fig. 19 Schematic (a) and SEM image (b) of the Edge Emission Laser Facet.

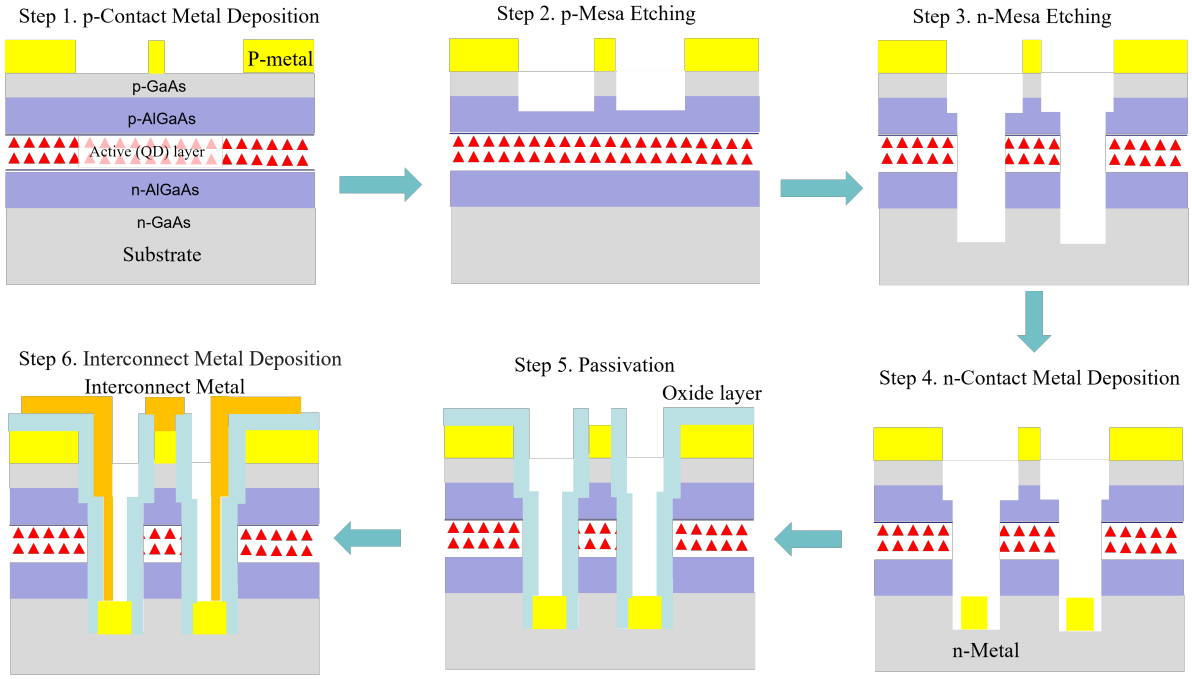

Fig. 20 Fabrication Flow for the Edge-Emission Waveguide Laser. The microelectronic process includes p-contact metal deposition, p-mesa etching, n-mesa etching, n-contact metal deposition, passivation and interconnect metal deposition.

5.1 Testing of Edge Emitting laser.

The Eq (27) is considered for fit curve of small signal response of highspeed performance [37]:

$$M(\omega) = \left(\frac{1}{1 + j\omega\tau_s}\right)\frac{A}{\omega_r^2 - \omega^2 + j\omega\gamma} \tag{27}$$

ω is resonant frequency = $2\pi f_r$, γ is damping factor, τ_s is the carrier transport/capture time and A

is amplification factor. $M(\omega)$ is signal response of frequency and $M(\omega) = S(\omega)/i$ for $S(\omega)$ equal output optical power with i equal to input current.

Consider about DC offset, the damping factor is defined as [35]:

$$\gamma = Kf_r^2 + \tau^{-1} \tag{28}$$

The τ is effective bimolecular recombination lifetime.

Thus,

$$K = \frac{\partial \gamma}{\partial f_r^2} \tag{29}$$

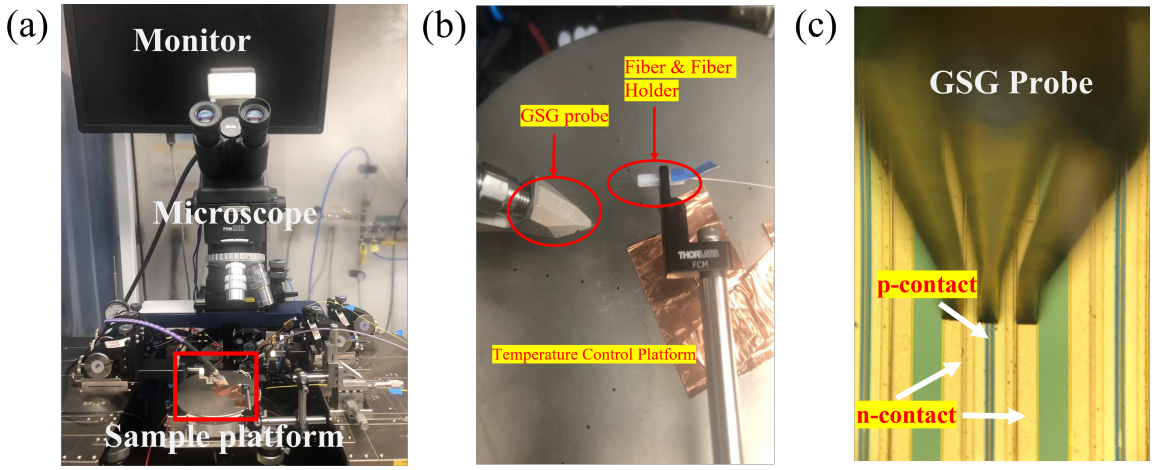

Fig. 21 Probe Station Setup for LIV and Speed Response Testing. (a) Probe station for optical and electrical testing, (b) zoomed-in picture for GSG probe and collection fiber. Injection current (DC and RF) is fed through the GSG probe, and output power is collected by a multimode fiber. (c) Alignment of GSG probe with electrodes of EEL.

We build a platform of probe station, shown in Fig. 21 (a), to characterize the electrical and optical performances of laser devices. Fig. 21 (b) shows the GSG probe and collection fiber. The electrical pumping current is fed into the laser device through the GSG probe and the laser emission from the cavity is collected with an optical fiber (as-cleaved facet, multi-mode). The electrical injection current is provided by the RF and DC sources going through a bias tee where the DC current creates the steady state working condition for the laser (above threshold current) and the RF works as a current perturbation to probe the speed response. Fig. 21 (c) shows the alignment of the GSG probe with the electrodes of the EEL device. The middle pitch of the GSG probe contacts the p-metal of the device and the other two pitches contact the n-metal of the device to create the current flow inside the waveguide EEL. The center small line in the microscope image is the p-contact metal and the two wide lines are the n-contact metal. The collected emission from the device is sent to an optical spectrum analyzer (OSA) to characterize the spectrum. A photon detector (Newport 1414 High Speed Fiber-Optic Detector) is used to convert the optical signal into electrical signal, which is then transmit into the light wave component analyzer (Agilent Technologies N4375D) to measure the laser speed response. The whole process is seamlessly automized by the LabView program.

We did the testing of LIV measurements, emission spectrum, and speed response. From the measurement results, we can extract the threshold current, threshold current density, K-factor, 3dB

bandwidth, and modulation efficiency for the EEL device. **Table 7**compares our testing results for ridge waveguides of several waveguide dimensions on an EEL sample (R303_A200915B, reported in [4]) with the references.

Table 7 Comparison of the Waveguide EEL Device Performances.

Cavity length L (μm)	Cavity Width w (μm)	Facets	I_{th} (mA)	J_{th} (kA/cm^2)	K (GHz^{-1})	-3dB BW (GHz)	Mod. Eff. GHz/mA$^{1/2}$	Reference
1500	5	HR/HR	10	0.13	1.288	5.1	0.66	[14]
580	3	HR/cleaved	14		0.92	6.5	0.68	[15]
	3 (UID*)	HR/cleaved	5.5		1.3	4.0	1.11	
500	4	As cleaved	70	3.5	0.367	4.07	0.496	This report
1000	5	As cleaved	20.8	0.416	1.685	3.73	0.399	
	6	As cleaved	15.6	0.26	1.011	4.18	0.391	
	8	As cleaved	26.8	0.335	1.968	3.75	0.440	
2000	3	As cleaved	20	0.333	1.022	4.42	0.649	
	4	As cleaved	18	0.225	0.910	5.58	0.487	
	5	As cleaved	33	0.330	0.843	5.24	0.480	

* UID means GaAs barrier after the QD layer was unintentionally doped.

Compared with EEL characterization results in the references, our testing results show a larger threshold current due to the coarser waveguide facets. Our speed response (e.g., K-factor, 3-dB bandwidth, and modulation efficiency) are very similar with the previous publications.

The plots in Fig. 22 are the LIV and speed response testing results of a ridge waveguide of 2mm in length and 4μm in width on an EEL sample (R303_A200915B). Fig. 22 (a) shows the LIV measurements of the 2mm-by-4μm EEL. The IV relations are obtained by the current-voltage outputs of the current source. The LI relations are measured by a power meter at different injection current levels. The spectra in Fig. 22 (b) are measured by injecting the optical emission into the OSA through a multimode fiber. The speed responses at different injection current are fitted with Eq. (24), as shown in Fig. 22 (c). Then we can derive the 3dB bandwidth in Fig. 22 (d), K-factor in Fig. 22 (e), and the modulation efficiency in Fig. 22 (f).

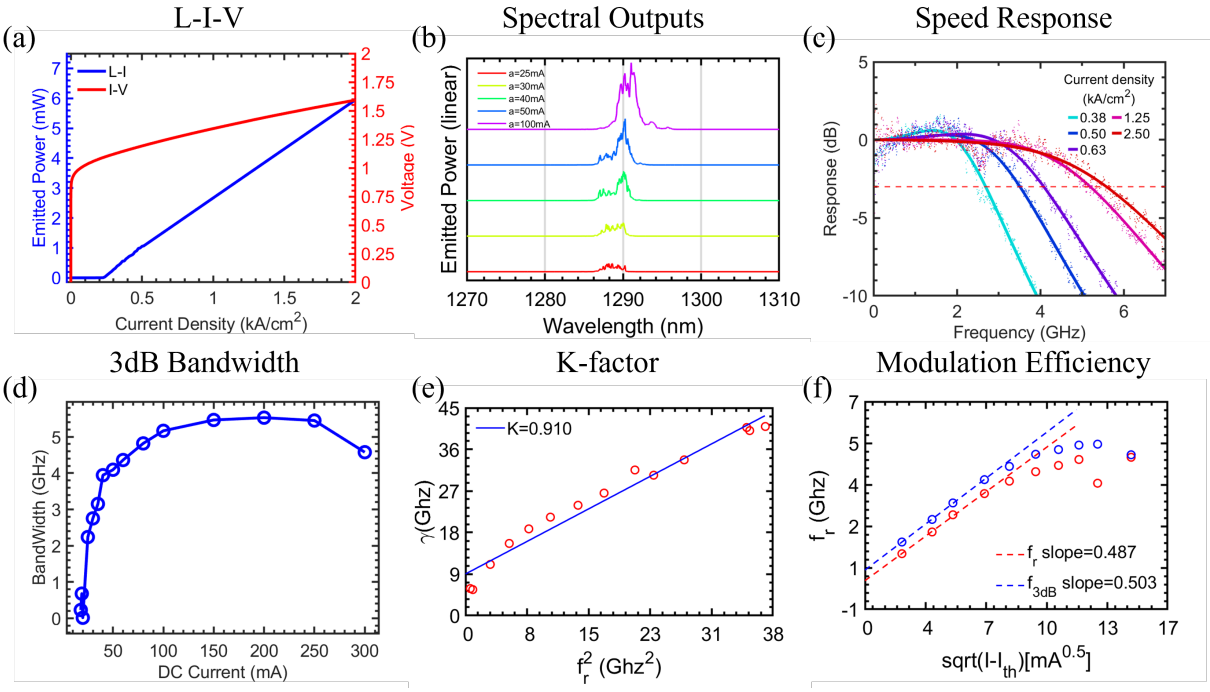

Fig. 22 LIV and speed response testing results for a 2 mm length and 4μm width ridge waveguide EEL. (a) L-I-V curve, (b) emission spectra (in linear scale) under different levels of DC injection current, (c) measured (dots) and fitted (solid lines) speed response at different injection current density, (d) 3dB bandwidth at different levels of DC injection current, (e) K-factor and (f) the corresponding modulation efficiency.

Reference:

1 'Dynamic Effects', Diode Lasers and Photonic Integrated Circuits, 2012, pp. 247-333

2 Shambat, G., Ellis, B., Petykiewicz, J., Mayer, M., Sarmiento, T., Harris, J., Haller, E., and Vuckovic, J.: 'Nanobeam photonic crystal cavity light-emitting diodes', Applied Physics Letters, 2011, 99, (7), pp. 71105-71105

3 Takeda, K., Fujii, T., Shinya, A., Notomi, M., Kakitsuka, T., and Matsuo, S.: '1-fJ/bit Direct Modulation of Photonic-Crystal Lasers', in Editor (Ed.)^(Eds.): 'Book 1-fJ/bit Direct Modulation of Photonic-Crystal Lasers' (2018, edn.), pp. 1-3

4 Joannopoulos, J.D., Villeneuve, P.R., and Fan, S.: 'Photonic crystals: putting a new twist on light', Nature, 1997, 386, (6621), pp. 143-149

5 Johnson, S.G., Fan, S., Villeneuve, P.R., Joannopoulos, J.D., and Kolodziejski, L.: 'Guided modes in photonic crystal slabs', Physical Review B, 1999, 60, (8), pp. 5751

6 Fan, S., and Joannopoulos, J.D.: 'Analysis of guided resonances in photonic crystal slabs', Physical Review B, 2002, 65, (23), pp. 235112

7 John D. Joannopoulos, S.G.J., Joshua N. Winn, and Robert D. Meade: 'Photonic Crystals: Molding the Flow of Light' (Princeton Univ. Press, 2008. 2008)

8 Zhou, W., Zhao, D., Shuai, Y.-C., Yang, H., Chuwongin, S., Chadha, A., Seo, J.-H., Wang, K.X., Liu, V., Ma, Z., and Fan, S.: 'Progress in 2D photonic crystal Fano resonance photonics', Progress in Quantum Electronics, 2014, 38, (1), pp. 1-74

9 Sauvan, C., Lecamp, G., Lalanne, P., and Hugonin, J.: 'Modal-reflectivity enhancement by geometry tuning in Photonic Crystal microcavities', Opt Express, 2005, 13, (1), pp. 245-255

10 Deotare, P.B., McCutcheon, M.W., Frank, I.W., Khan, M., and Loncar, M.: 'High quality factor

photonic crystal nanobeam cavities', Appl Phys Lett, 2009, 94, (12), pp. 121106
11 Burek, M.J., Chu, Y., Liddy, M.S., Patel, P., Rochman, J., Meesala, S., Hong, W., Quan, Q., Lukin, M.D., and Loncar, M.: 'High quality-factor optical nanocavities in bulk single-crystal diamond', Nat Commun, 2014, 5, (1), pp. 5718
12 Shambat, G., Ellis, B., Petykiewicz, J., Mayer, M.A., Sarmiento, T., Harris, J., Haller, E.E., and Vuckovic, J.: 'Nanobeam photonic crystal cavity light-emitting diodes', Appl Phys Lett, 2011, 99, (7), pp. 071105
13 Yang, D., Liu, X., Li, X., Duan, B., Wang, A., and Xiao, Y.: 'Photonic crystal nanobeam cavity devices for on-chip integrated silicon photonics', Journal of Semiconductors, 2021, 42, (2), pp. 023103
14 Trivino, N.V., Butte, R., Carlin, J.F., and Grandjean, N.: 'Continuous wave blue lasing in III-nitride nanobeam cavity on silicon', Nano Lett, 2015, 15, (2), pp. 1259-1263
15 Jeong, K.-Y., No, Y.-S., Hwang, Y., Kim, K.S., Seo, M.-K., Park, H.-G., and Lee, Y.-H.: 'Electrically driven nanobeam laser', Nature Communications, 2013, 4, (1), pp. 2822
16 He, Z., Chen, B., Hua, Y., Liu, Z.J., Wei, Y.M., Liu, S.F., Hu, A., Shen, X.Y., Zhang, Y., Gao, Y.A., and Liu, J.: 'CMOS Compatible High-Performance Nanolasing Based on Perovskite-SiN Hybrid Integration', Advanced Optical Materials, 2020, 8, (15), pp. 2000453
17 Yang, Z., Pelton, M., Fedin, I., Talapin, D.V., and Waks, E.: 'A room temperature continuous-wave nanolaser using colloidal quantum wells', Nat Commun, 2017, 8, (1), pp. 143
18 Shakoor, A., Nozaki, K., Kuramochi, E., Nishiguchi, K., Shinya, A., and Notomi, M.: 'Compact 1D-silicon photonic crystal electro-optic modulator operating with ultra-low switching voltage and energy', Opt Express, 2014, 22, (23), pp. 28623-28634
19 Javid, M.R., Miri, M., and Zarifkar, A.: 'Design of a compact high-speed optical modulator based on a hybrid plasmonic nanobeam cavity', Optics Communications, 2018, 410, pp. 652-659
20 Hadian Siahkal-Mahalle, B., and Abedi, K.: 'Ultra-compact low loss electro-optical nanobeam cavity modulator embedded photonic crystal', Optical and Quantum Electronics, 2019, 51, (5), pp. 128
21 Cheng, Z., Dong, J., and Zhang, X.: 'Ultracompact optical switch using a single semisymmetric Fano nanobeam cavity', Opt Lett, 2020, 45, (8), pp. 2363-2366
22 Soref, R., and Hendrickson, J.: 'Proposed ultralow-energy dual photonic-crystal nanobeam devices for on-chip N x N switching, logic, and wavelength multiplexing', Opt Express, 2015, 23, (25), pp. 32582-32596
23 Meng, Z.M., Chen, C.B., and Qin, F.: 'Theoretical investigation of integratable photonic crystal nanobeam all-optical switching with ultrafast response and ultralow switching energy', J Phys D Appl Phys, 2020, 53, (20), pp. 205105
24 Yang, D.Q., Kita, S., Liang, F., Wang, C., Tian, H.P., Ji, Y.F., Loncar, M., and Quan, Q.M.: 'High sensitivity and high Q-factor nanoslotted parallel quadrabeam photonic crystal cavity for real-time and label-free sensing', Appl Phys Lett, 2014, 105, (6), pp. 063118
25 Dong, P., Qian, W., Liang, H., Shafiiha, R., Feng, N.N., Feng, D., Zheng, X., Krishnamoorthy, A.V., and Asghari, M.: 'Low power and compact reconfigurable multiplexing devices based on silicon microring resonators', Opt Express, 2010, 18, (10), pp. 9852-9858
26 Dong, P., Qian, W., Liang, H., Shafiiha, R., Feng, D., Li, G., Cunningham, J.E., Krishnamoorthy, A.V., and Asghari, M.: 'Thermally tunable silicon racetrack resonators with ultralow tuning power', Opt Express, 2010, 18, (19), pp. 20298-20304
27 Zhang, J., and He, S.: 'Cladding-free efficiently tunable nanobeam cavity with nanotentacles', Opt Express, 2017, 25, (11), pp. 12541-12551
28 Srinivasan, K., Borselli, M., and Painter, O.: 'Cavity Q, mode volume, and lasing threshold in small diameter AlGaAs microdisks with embedded quantum dots', Optics Express, 2006, 14, (3), pp. 1094-1105
29 Ellis, B., Mayer, M., Shambat, G., Sarmiento, T., Harris, J., Haller, E., and Vuckovic, J.: 'Ultralow-threshold electrically pumped quantum-dot photonic-crystal nanocavity laser', Nature Photonics, 2011, 5, (5), pp. 297-300
30 Zhang, Y., McCutcheon, M., Burgess, I., and Loncar, M.: 'Ultra-high-Q TE/TM dual-polarized

photonic crystal nanocavities', Optics Letters, 2009, 34, (17), pp. 2694-2696
31 Quan, Q., and Loncar, M.: 'Deterministic design of wavelength scale, ultra-high Q photonic crystal nanobeam cavities', Opt Express, 2011, 19, (19), pp. 18529-18542
32 Oskooi, A.F., Roundy, D., Ibanescu, M., Bermel, P., Joannopoulos, J.D., and Johnson, S.G.: 'MEEP: A flexible free-software package for electromagnetic simulations by the FDTD method', Computer Physics Communications, 2010, 181, (3), pp. 687-702
33 'Gain and Current Relations', Diode Lasers and Photonic Integrated Circuits, 2012, pp. 157-246
34 Matsuo, S., and Kakitsuka, T.: 'Low-operating-energy directly modulated lasers for short-distance optical interconnects', Advances in Optics and Photonics, 2018, 10, (3), pp. 567-643
35 Tao, L., Wang, Y., Gao, Y., Lau, A., Chi, N., and Lu, C.: 'Experimental demonstration of 10 Gb/s multi-level carrier-less amplitude and phase modulation for short range optical communication systems', Optics Express, 2013, 21, (5), pp. 6459-6465
36 Pan, M., Liu, Z., Kalapala, A.R.K., Chen, Y., Sun, Y., and Zhou, W.: 'Complete 2 {\pi} Phase Control by Photonic Crystal Slabs', arXiv preprint arXiv:2108.01160, 2021
37 Nagarajan, R., Ishikawa, M., Fukushima, T., Geels, R.S., and Bowers, J.E.: 'High speed quantum-well lasers and carrier transport effects', IEEE Journal of Quantum Electronics, 1992, 28, (10), pp. 1990-2008